INTERROGATION OF MID-BUILD INTERNAL TEMPERATURE DISTRIBUTIONS WITHIN PARTS BEING MANUFACTURED VIA THE POWDER BED FUSION PROCESS

Nathaniel Wood[1], Heimdall Mendoza[2], Paul Boulware[2], and David J. Hoelzle [*][1]

[1]Department of Mechanical and Aerospace Engineering, the Ohio State University, Columbus, OH 43210
[2]EWI, Columbus, OH, 43221

Abstract

This work reports on the measurement of the internal temperature distributions of parts being manufactured via the Powder Bed Fusion (PBF) process. Eight test coupons were machined from a piece of wrought 304 stainless steel (SS). Thermocouples were inserted into the test coupon interiors to sample internal thermal history. The coupons were then placed into the open architecture laser PBF machine housed at EWI and covered to their uppermost surfaces with 316 SS powder. Three tests were executed: First, the laser rastered over the coupons without inducing melting. Second, the laser rastered over the coupons while melting the exposed faces. Lastly, five layers of 316 SS were built atop the coupons. The main result is a comprehensive data set of a multitude of measured physical inputs and outputs under typical build conditions: embedded thermocouple temperatures, laser centroid, laser power, and infrared imagery of the exposed coupon faces.

1 Introduction

Powder Bed Fusion (PBF) belongs to a class of manufacturing processes known as *additive manufacturing* (AM). The PBF process builds 3-D parts out of layers of metal powder using a build cycle consisting of three stages: 1) sweeping of a thin layer of powder over a base plate or previously applied powder, 2) selectively melting a 2-D pattern of desired geometry into the powder by application of a high-powered laser or electron beam, and 3) lowering the build platform in the $-z$ direction to accommodate a fresh layer of powder. Fig. 1 demonstrates the PBF architecture.

Of interest to the PBF community is the validation of temperature predictions supplied by PBF process models, which may be used to better predict the formation of common defects such as
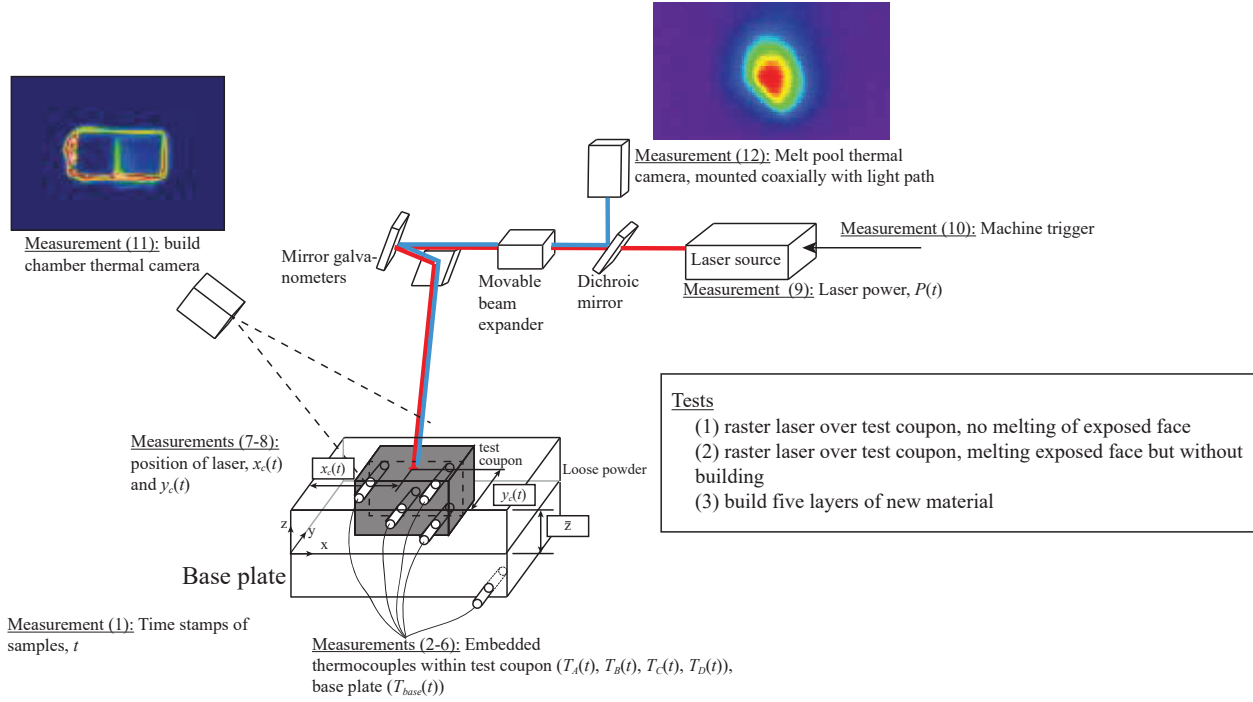

Figure 1: **Schematic of experimental setup and measurements.** Objective of experiment is to sample internal temperature distributions within simulated mid-build PBF conditions under a range of increasingly complex modes of heat transfer. Measurements 1-10 were collected with data acquisition system (DAQ) and stored as a single array. Measurements 11-12 were stored as separate video files. Representative images of Measurements 11-12 taken from experimental data.

high levels of residual stresses [1–3], porosity [4–6], and anisotropy in material properties [6–11]. The general Laser Powder Bed Fusion (L-PBF) model validation task is as follows: Given a part geometry, termed coupon here, and process inputs and parameters, qualitatively or quantitatively compare a set of measurable process outputs to process outputs predicted by a model. These validations a critically important task for researchers in the field and is accomplished through taking in-situ temperature data of the process. We now give a brief sampling of such efforts and discuss the limitations of the strategies employed therein.

In-situ temperature measurements are typically gathered with IR camera measurements of the exposed build surface [12, 13]. Less commonly available are studies which validate models of sub-surface temperature distributions by directly measuring these subsurface temperatures with thermocouples (TCs) embedded in the base plate adjacent to and/or underneath the coupon [14–19]. Regardless of strategy, works presenting validations of PBF heat transfer models typically only provide plots of the data in a journal article, not the raw data itself. Additionally, nominal process inputs and parameters are often provided; however, the actual input often deviates from nominal and thus measurements of these inputs provide a more realistic understanding of the input that should be provided to the process model. These practices hurt the community's ability to replicate the authors' analysis and precisely reproduce the exact process inputs corresponding to the observed data when validating their own models.

Additionally, validations performed with embedded TCs typically lack repeat measurements, i.e., multiple measurements taken during the same experimental run. For example, [15, 17, 18, 18, 19] use only two TCs in their experimental apparatus, and [14, 16] use three. [16], which studied Direct Energy Deposition (DED), embedded one of the TCs inside the coupon itself. These validation strategies also typically lack replicate measurements, ie data from multiple experiments with the same setup. Of the aforementioned studies, only [16, 17] used more than one test coupon when validating their models, providing a visual representation of two and three two and three coupons, respectively. Such limited quantities of data limit the application of statistical tools that account for the presence of experimental uncertainty. The typical far-afield placement of the embedded TCs further compounds this uncertainty due to the negative effect of distance on the information content carried by the TC signals regarding melt pool and heat affected zone dynamics.

Finally, the coupons employed when validating PBF thermal models are typically simplistic. [13, 17] validated their models by fusing a single layer of powder to the base plate. [12, 18, 19] employed cuboid geometries. Researchers studying DED typically validate their thermal models on thin wall coupons, as in [14–16]. Validating models using such simple geometries presents a set of model boundary conditions that fail to reflect realistic build scenarios and thus limit the validations' applicability to predicting process dynamics in real-world contexts.

The purpose of this paper is to supply an exhaustive dataset containing sampled internal temperature dynamics and corresponding process inputs and outputs of the PBF process along with a complete description of the associated experimental procedures, for direct validation of PBF thermal models. Fig. 1 demonstrates the basic architecture of the experiment and the experiment outputs. We performed this experiment on the open architecture PBF machine at EWI, which provided our team with full access to all process inputs and outputs. The experiment consisted of rastering a laser sequentially over eight test coupons that were raised above a base plate and instrumented with TCs. Coupons 1-4 featured a simple cuboid geometry, while coupons 5-8 featured an I-beam shaped cross section. This approach provides four replicates for both coupon architectures under consideration. Additionally, positioning TCs symmetrically in the northeast (NE) and northwest (NW) corners of the coupons as shown in Fig. 1 generates two repeats within each coupon due to the rastering laser exciting them identically. The large number of repeats and replicates offered by our experiment increases the effectiveness of statistical tools when accounting for experimental uncertainty in our data. Additionally, we carried out our testing on all coupons in three stages, as detailed in Fig. 2 and Table 1 and denoted hereafter as "Tests:" Test 1 heated the exposed coupon surfaces beneath melting temperature, Test 2 melted the coupon surfaces, and Test 3 built five layers of material on the coupon surfaces. Each Test induced more complex modes of heat transfer, thus affording opportunities to analyze the effect of complex cross-sectional geometries on nonlinear PBF process dynamics. During each Test, for each coupon, we collected the following signals: four TC signals from TCs embedded within the coupon, a TC signal corresponding to a TC embedded far afield in the base plate as shown in Fig. 1, X and Y position signals of the laser centroid, the signal governing the laser power, coaxial IR camera footage of the melt pool, off-axis IR camera footage of the build chamber and a machine trigger signal that synchronized all other data streams. The galvanometer and power process input signals may be integrated into PBF thermal models to more accurately compare predicted process dynamics and outputs against the measured dynamics and outputs provided by our data. We make this data publicly available as
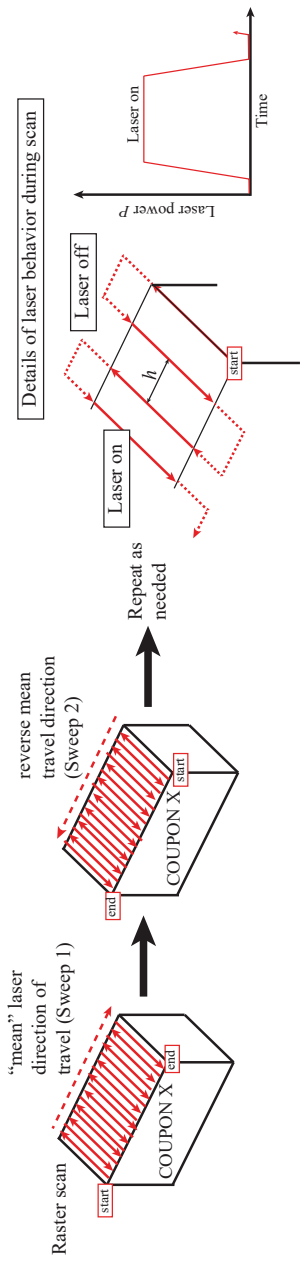
Figure 2: **Laser scan path used during experiments.** Specific scan parameters given in Tb. 1.

detailed in Table 4.

Table 1: Experimental process parameters

	Stage					High temp. emissivity calibration
	1A	1B	1C	2	3	
Max scan speed, v (mm/s)					960	
Laser spot size, σ (μm)					100	100
Hatch spacing, h (μm)					100	
Layer thickness, d (μm)				-	40	-
Nominal laser power, P_{nom} (W)	6.875	13.75	20.625	275	275	30
Number of sweeps, s (–)	5	5	5	5	1	100

2 Experimental Setup

2.1 PBF Machine overview

All experiments were performed on an open-architecture L-PBF housed at EWI. Laser path planning is fully programmable at the machine level. Motion control I/O is available for sensor triggering, synchronization, and position tracking. The laser optical path is open to an optical table, reconfigurable for different sensory tooling to take measurements through the laser beam axis. The build chamber includes five viewing ports (3 top, 1 front, 1 side), internal 80-20 mounting bars, and hole patterns on the recoating arm all for sensor mounting. Roxtec cable channels are used for routing auxiliary sensor cables into the chamber. A gas orifice provides a stream of gas overtop the exposed surface of the test build being conducted to remove vapor and spatter from the test build vicinity. This architecture allows the pursuit of research and development objectives which require the ability to manipulate the process itself and demand real-time process characterization, unlike commercial machines in which path planning, motion control, optical path, and the build chamber are under restricted access.

2.2 Test part design

Here we present the geometry, TC integration, and material selection and rationale of the part used during our experiment, hereafter referred to as the "test part." Fig. 3 displays the test part, which takes the form of a base plate with eight raised test coupons and assorted sacrificial coupons machined from a single piece of 304 stainless steel (SS). Each coupon represents a partially-completed part, which allows us to emulate mid-build PBF internal temperature distributions and measure temperature at specific spatial locations inside the part. Appendix B displays the dimensions of the part, the measured dimensions of the part as performed by the fabricators and photographs of the part inside the experimental setup, labeled as necessary with part numbers and numbering conventions. TCs were embedded in the coupon holes and labeled according to the convention given in Fig. 3. Fig. 15 shows the test part after TC insertion.

Three factors governed the choice of test part geometry as shown in Fig. 3:

1. **Sample from a multitude of spatial locations.** Each coupon had four integrated TCs, measuring temperature near the top surface (A and B), geometric center (C), and near the base plate (D). The symmetric placement of TCs A and B within all coupons as shown in Fig. 3 measured identical excitement from the rastering laser and thus constituted repeat measurements.

2. **Multiple coupon architectures** Four of the test coupons (5-8, as shown in Fig. 3) were constructed with an I-beam structure instead of as simple cuboids to better investigate the role of complex geometry in PBF heat transfer.

3. **Replicate measurements.** Each design was repeated four times to provide four independent measurements to assess process variability. These coupons were configured on the perimeter of the test part to accommodate the build chamber IR camera FOV and machining limitations. Rotating the test part by 180° clockwise brought coupons 5-8 into the build chamber IR camera's FOV. These test part configurations within the PBF machine are shown in Fig. 16b and Fig. 17a.

Omega TJ36-CASS-020E-6 TCs were inserted into the holes marked A-D for all coupons as shown in Fig. 3, which are Type K TCs with exposed junctions and 304 SS sheathes. This TC model was chosen because its 0.5 mm sheath diameter provides a minimal sensor time constant and footprint on the surrounding coupon heat transfer within machining constraints. Based on consultation with Omega Engineering, the time constant for these TCs was expected to be roughly 75 ms. TC locations A and B were selected to be the minimal feasible distance from the NE and NW coupon corners for 0.6 6mm diameter holes having a depth of 2.5 mm, as determined by consultation with machinists. The TCs were held in place with Omega OB-600 high temperature cement. The TC embedded into the build plate was a standard Type K TC with an ungrounded junction and 304 SS sheath, Omega TJ36-CASS-18U-6.

The test part was constructed from 304 SS in order to match the sheath material of the embedded TCs. For all tests, the part was immersed in 316L SS powder and for Test 3 the part was

covered in a thin (40 μm, Table 1) layer of powder. 316L SS was used as it is a commonly used stainless steel available in powdered form for L-PBF. As Table 2 shows, the thermal properties of 316L SS and 304 SS are in good agreement over a wide range of temperatures and therefore we assumed that the material mismatch would not induce appreciable heat transfer artifacts.

Table 2: Comparison between thermal properties of 304 and 316L SS [20]

Property	symbol	304 SS	316L SS
density (kg/m^3)	ρ	7920-8070 (0-100 ^{o}C)	7860-8020 (0-100 ^{o}C)
specific heat (J/kg-K)	c_p	500-640 (20-927 ^{o}C)	500-630 (20-700 ^{o}C)
thermal conductivity (W/m-K)	k	16.0-24.0 (100-627 ^{o}C)	16.0-23.0 (100-700 ^{o}C)

2.3   Non-IR signal acquisition

Here we describe procedures for acquiring all non-IR camera data. Fig. 4 displays the signal acquisition pathways used throughout our experiments. The signals stored in the DAQ output array are sampled at 1000 Hz and ordered as follows:

1. Time stamp, t.

2–5) Temperature readings from TCs TCA-TCD for the coupon being tested, respectively, denoted as $T_A(t)$ through $T_D(t)$. (analog)

6. Temperature readings from the base plate TC, denoted as $T_{base}(t)$. (analog)

7. X-coordinate of the laser centroid, denoted as $x_c(t)$ (analog). This measurement was collected from the position of the corresponding galvanometer, hereafter referred to as the "X-Galvo." Data converted from units of volts to mm via calibration map.

8. Y-coordinate of the laser centroid, denoted as $y_c(t)$ (analog). This measurement was collected from the position of the corresponding galvanometer, hereafter referred to as the "Y-Galvo." Data converted from units of volts to mm via calibration map.

9. Laser power, denoted as $P(t)$. (analog)

10. Trigger signal used to synchronize all data streams (digital).

The TC voltage signals were amplified with two PlayingWithFusion SEN-30101/K1 TC amplifier boards, which feature a 50 kHz bandwidth. Correlation tables supplied by the manufacturer related the measured voltage to temperature. The amplifiers were powered by an HQ Power PS23003AU DC power supply. As shown in Fig. 4, each TC lead was passed out of the machine through an air tight Roxtec port. These leads are Omega TT-K-24-TWSH shielded TC cables with Omega GMP-K-F(M) TC connectors, shielded according to [21].
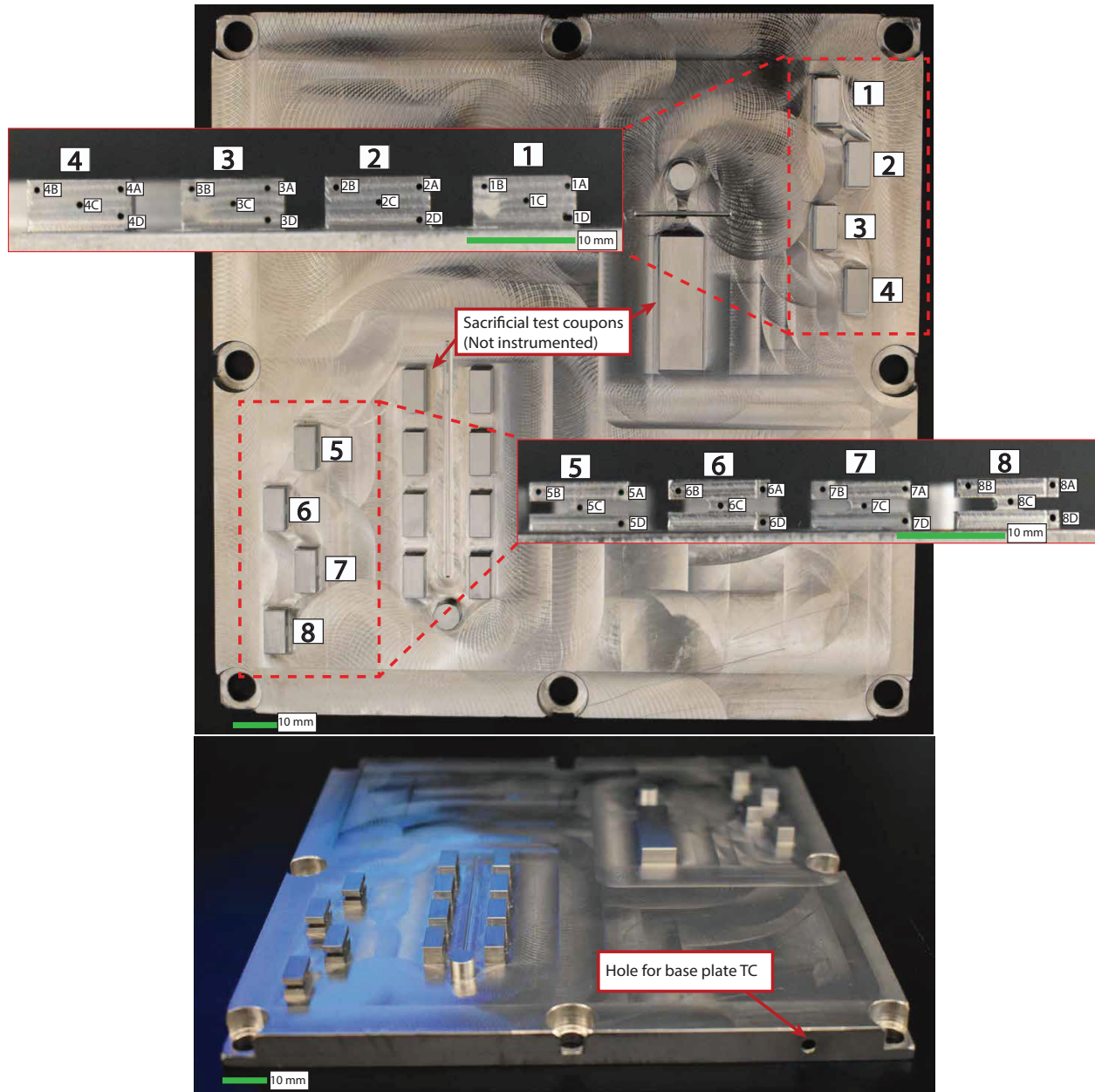
Figure 3: Test part used to conduct experiment, showing the numbering convention for the associated test coupons and TC holes.

Cables carrying the X-Galvo, Y-Galvo and laser power signals were run out of the open architecture PBF machine hardware and fed directly into the DAQ. The correlations between galvanometer signal (V) and laser position (mm), and laser power signal (V) and power (W) are

linear:

$$x_c(t) : 125\,\text{mm/V}$$
$$y_c(t) : 125\,\text{mm/V}$$
$$P(t) : 175\,\text{W/V}. \tag{1}$$

The native 24V machine trigger signal was stepped down to a 5V signal by means of an Allen Bradley 700-TBS24 solid state relay, as shown in Fig. 4, so as to not saturate the DAQ. The pickup time for this relay is 30 μs, which is is beneath our sampling period of 1 ms and thus incurred no signal lag. A 10 ms delay between the trigger activation and laser activation was inserted into the G-code to ensure that any transient dynamics in the startup of various machine components had settled prior to beginning the test and thus could not introduce artifacts in the data.

2.4   IR camera signal acquisition

The EWI PBF machine was equipped with two IR cameras: a Stratonics HSTV camera (the "melt pool camera") which had a FOV of the melt pool and a Micro-Epsilon TIM 640 camera (the "build chamber camera") which had a FOV covering the NE quadrant of the test part (Fig. 3). The melt pool camera camera operates with dual-color pyrometery and thus required no emissivity calibrations to function, having an emissivity-independent calibration curve given in Appendix A. The build chamber camera uses single color pyrometery and therefore necessitated emissivity calibrations of the coupon metal and surrounding powder. These calibration procedures are discussed in Appendix A. Both cameras were triggered by the same trigger signal described in the previous section and stored with proprietary software for each respective camera. The Micro-Epsilon camera has a maximum framerate of 30 Hz. The Stratonics camera has a maximum framerate of 10 kHz, however RAM limitations within the camera imposed a strict 1000 sample limit with the default FOV before the system exhausted its memory, thus collecting only 0.1s of data. For this reason, the FOV of the camera was slightly reduced to allow the acquisition of 3000 samples and the sampling rate was reduced from 10 kHz to 1 kHz to allow for three seconds of data acquisition. Three seconds of footage corresponds to capturing 46% of data from Tests 1-2, which used five sweeps, and 100% of data from Test 3, which used one. The 960 mm/s laser traversed the 5mm coupon widths at a rate of 192 Hz and completed one 10 mm sweep in approximately 1.31 s. Sampling at 1000 Hz thus satisfied the Nyquist criteria for capturing the melt pool temperature data. However the build chamber camera, which sampled at 30 Hz, could not capture traversing the coupon widths and was restricted by Nyquist limitations to capturing the "mean" laser direction (Fig. 2) dynamics. Additionally, it was found during testing that the melt pool camera included 14 "dead" frames at the start of every acquisition in which no melt pool was visible despite the camera being active. No means of disabling or reducing this dead frame count were found. As a consequence the melt pool camera data does not capture the beginning of each raster scan.

3 Experimental Procedures

The experiment procedures are summarized below and will be discussed in more detail within the following Tests. Prior to running these Tests, basic calibration and identification of proper operating parameters was performed. Critically, we identified a minimum melting power, P_{min}, at which the laser can raster continually without melting the top surface, and a nominal power, P_{melt}, at which PBF printing is performed.

Test 1: Raster the laser overtop a coupon at a laser power beneath that required to melt the metal, while the part is immersed in powder.

   1A) Run laser power at 6.875 W, or 25% of P_{min}.

   1B) Repeat with laser power at 13.75 W, or 50% of P_{min}.

   1C) Repeat with laser power at 20.625 W, or 75% of P_{min}.

Test 2: Raster the laser overtop a coupon at a laser power set to 275 W (P_{melt}), while the part is immersed in powder.

Test 3: Build five layers of 316L SS on top of a coupon.

Tests 1-3 were first completed on coupons 1-4, and then repeated for coupons 5-8 after rotating the block as described in Section 2, so as to minimize the number of part rotations and, by extension, damage to the fragile TCs. Unlike Test 1, Tests 2 and 3 were irreversible because we wanted to preserve the microsctructures obtained by melting and fusing material, which eliminated the possibility of remelting.

Laser scans during all Tests followed the scan configuration shown in Fig. 2 and Table 1. All scan parameters except P_{nom} and s were held constant. Fig. 2 details the laser behavior during each sweep. A "sweep" was defined as rastering through the complete length of the coupon in one direction.

3.1 Tests 1 and 2: scanning without building

Tests 1 and 2 were carried out on coupons 1-4 by performing the corresponding laser scans defined in Fig. 2 and Table 1 sequentially on each coupon while collecting all data streams. Both Tests 1 and 2 were carried out in succession on each coupon before proceeding to the next. Fig. 16b shows the configuration of the test part setup when completing these tasks. After completion of Tests 1-3 on coupons 1-4, the test part was rotated to construct the configuration shown in Fig. 17a. Tests 1 and 2 were carried out on coupons 5-8 using the same procedure as done for coupons 1-4. Table 3 lists the filenames given to all data collected during Tests 1 and 2.

3.2 Test 3: five layer build

After the completion of Tests 1-2 on coupons 1-4, the top surfaces of the coupons were covered by powder as shown in Fig. 16c with a sweep of the recoater blade. Test 3 then was carried out on coupons 1-4. This consisted of performing the corresponding laser scan defined in Fig. 2 and Table 1 sequentially on each coupon while collecting all data streams. After material was fused on all four coupons, the build platform was dropped in the negative z direction and a new layer of powder was applied. This procedure was repeated until five layers of new material were fused on top of coupons 1-4. After rotation of the part and completion of Tests 1-2 on coupons 5-8, the top surfaces of coupons 5-8 were covered by powder as shown in Fig. 17b with a sweep of the recoater blade. Test 3 then was carried out on coupons 5-8 using the same procedure as done for coupons 1-4. Table 3 lists the filenames given to all data collected during Test 3.

Table 3: Filenames for data from each test. X denotes coupon number.

Test		DAQ (extension ".mat")	build chamber camera (extension ".ravi")	melt pool camera (frames stored in file folder)
	1A	Test_1_25_pX_DAQ	Test_1_25_pX_build_camera	Test_1_25_pX_melt_camera
Test 1	1B	Test_1_50_pX_DAQ	Test_1_50_pX_build_camera	Test_1_50_pX_melt_camera
	1C	Test_1_75_pX_DAQ	Test_1_75_pX_build_camera	Test_1_75_pX_melt_camera
Test 2		Test_2_pX_DAQ	Test_2_pX_build_camera	Test_2_pX_melt_camera
	Layer 1	Test_3_layer_1_pX_DAQ	Test_3_layer_1_pX_build_camera	Test_3_layer_1_pX_melt_camera
	Layer 2	Test_3_layer_2_pX_DAQ	Test_3_layer_2_pX_build_camera	Test_3_layer_2_pX_melt_camera
Test 3	Layer 3	Test_3_layer_3_pX_DAQ	Test_3_layer_3_pX_build_camera	Test_3_layer_3_pX_melt_camera
	Layer 4	Test_3_layer_4_pX_DAQ	Test_3_layer_4_pX_build_camera	Test_3_layer_4_pX_melt_camera
	Layer 5	Test_3_layer_5_pX_DAQ	Test_3_layer_5_pX_build_camera	Test_3_layer_5_pX_melt_camera

3.3 Unexpected events

This section covers events which occurred during testing that resulted in the unexpected alteration of the test setup or an accidental loss of data. These events must be factored into any conclusions drawn from this data set. Appendix B tabulates which measured data are available for which Tests.

1. Calibrating the high-temperature emissivity of the unwelded material as described in Appendix A altered the microstructure of coupon 3, discoloring it to be visibly darker than coupons 1, 2, and 4. This alteration of the coupon emissivity resulted in more efficient laser heat absorption than coupons 1, 2, and 4 and thus demonstrated higher temperature values for the same process inputs.

2. TC insertion and retention in their respective holes was delicate and led to errors. Three TCs came loose during the experiment and were not able to be replaced because the hole was plugged with cement. Accordingly, the dataset is missing TC data for 3D, 4B, and 6B.

3. The emissivity measurement for welded metal powder was first attempted on coupons 1-3 prior to coupon 4, but a combination of mistakes prevented this data from being recorded. This emissivity calibration required holding the coupons at elevated temperature and therefore may present artifacts in the final coupon microstructures.

4. The build chamber heater design unexpectedly provided nonuniform heating to the build plate. Accordingly, the single build plate TC shown in Fig. 3 did not permit accurate measurement of the build plate temperature for coupons 5 - 8. The base plate TC was moved to the placement shown in Fig. 17C to better measure the base plate temperature near coupons 5 - 8.

5. An unexpectedly high amount of background noise was encountered in the laser power signal when testing coupons 5-8. A set of data for zero nominal laser power was collected to characterize this noise for signal filter application. This data is provided as a part of the "Calibration studies" data set of Table 4 as "5-8_laser_background.mat."

6. The melt pool camera frame storage limitation discussed in Section 2 was only caught after performing Tests 1 and 2 on both coupons 1 and 2. These tasks were repeated for these two coupons, and emissivity values were re-taken.

7. The melt pool camera crashed during the following tests:

   - Test 2, coupon 4
   - Test 3, layer 4, coupon 4
   - Test 3, layer 3, coupon 5

   No melt pool temperature data was recorded for these tests.

8. 5 sweeps were mistakenly ran instead of 1 sweep overtop coupon 8 for Test 3, layer 1.

3.4 Data storage

All data from this experiment is stored on Amazon Web Services (AWS), which is a publicly-available archive. The data is divided into ten files that represent each test performed. Table 4 displays the download links for this data.

Table 4: Download links for experimental data

Test		download link
Calibration studies		http://hrl-pbf-thermal-validation-study.s3.amazonaws.com/calibration_data.zip
	1A	http://hrl-pbf-thermal-validation-study.s3.amazonaws.com/test_1a.zip
Test 1	1B	http://hrl-pbf-thermal-validation-study.s3.amazonaws.com/test_1b.zip
	1C	http://hrl-pbf-thermal-validation-study.s3.amazonaws.com/test_1c.zip
Test 2		http://hrl-pbf-thermal-validation-study.s3.amazonaws.com/test_2.zip
	Layer 1	http://hrl-pbf-thermal-validation-study.s3.amazonaws.com/test_3_layer_1.zip
	Layer 2	http://hrl-pbf-thermal-validation-study.s3.amazonaws.com/test_3_layer_2.zip
Test 3	Layer 3	http://hrl-pbf-thermal-validation-study.s3.amazonaws.com/test_3_layer_3.zip
	Layer 4	http://hrl-pbf-thermal-validation-study.s3.amazonaws.com/test_3_layer_4.zip
	Layer 5	http://hrl-pbf-thermal-validation-study.s3.amazonaws.com/test_3_layer_5.zip

4   Experimental Results

In this section we present results pertaining to measured material emissivity ε, measured TC data $T_A(t)$-$T_{base}(t)$, measured centroid position data $x_c(t)$ and $y_c(t)$, measured power $P(t)$, and IR camera footage. We present TC data from Tests 1-3 for coupons 1 and 5, which display typical results for all TC data collected and are thus used as representative examples. Similarly, $P(t)$, $x_c(t)$, $y_c(t)$ signals gathered from Test 2, coupon 1 is presented as typical of data gathered from these coupons during the experiment. This was done for the sake of brevity, as the entire dataset is exhaustive; encompassing Tests 1-3 for all 8 coupons and all 12 data streams.

4.1   Emissivities

Table 5 lists ε measured at specific time points during the experiments, as measured according to the procedures given in Appendix A. These results show that the welded metal powder had the highest ε, followed by the wrought steel, with the laser treated steel having the lowest. Coupon 3 was recorded as an exception to the rule as explained in Section 3.3. The high ε of the welded metal powder is in agreement with the knowledge that 304 SS ε increases as surface roughness increases [22, 23] and that the surface roughness of parts manufactured via PBF are rough [4].

Table 5: Emissivity ε calibration values. "Applicable Test" refers to the Tests in which the given material type appears.

Material type	Applicable Test	Low temp. ε (temperature)	High temp. ε (temperature)
Powder	1, 2, 3	0.440 (331.2 K)	–
Wrought steel	1, 2	0.075 (334 K)	0.120 (823.2 K)
Laser treated steel, coupon 2	2, 3	0.10 (342.7 K)	0.010 (863.2 K) (lower saturation limit reached)
Laser treated steel steel, coupon 3	2,3	0.70 (345.9 K)	0.09 (773.2 K)
Welded powder surface	3	0.115 (343.2 K)	0.20 (873.2 K)

4.2   Representative results: TC data

Here we show representative TC data from Tests 1 - 3. For Tests 1 - 2, the raw temperature signal from either coupon 1 or 5 is shown, with the envelope of replicated experiments shaded behind the raw signal (Fig. 5, 6). Only the raw data from coupons 1 and 5 are shown for Test 3 for clarity. The labels TCA-TCD follow the convention outlined in Fig. 3.

Temperature data for Test 1 and 2 (Fig. 5-6) share a common trend of TCs A and B demonstrating temperature peaks which alternate in time and TCC sharing temperature peaks of both TCA and TCB. This trend is explained in Fig. 7. As the laser sweeps across the length of the coupon, the laser passes over TCA (or TCB) twice in quick succession, yielding a single oberved peak. Since TCC is in the middle of the part, the duration between laser passes is longer and thus a peak is observable at each pass. The temperature signals produced by the three power levels of Test 1 were similar for both coupons 1 and 5, which may be due to the presence of inconsistent

laser power at low laser powers as demonstrated in Fig. 10. The unusually low initial signal from TC 5B may be attributable to artifacts induced by re-inserting the TC into its connection after it was dislodged during part rotation, or due to the proximity of coupon 5 to the position of the gas orifice during testing shown Fig. 16a.

Fig. 8 demonstrates representative TC data from coupons 1-4 for Test 3, while Fig. 9 does the same for coupon 1-5 Test 3 data. Coupons 1 and 5 displayed opposing trends over the course of their five layer builds: As additional layers were built on coupon 1 the TCs measured lower temperatures, whereas when the same was done to coupon 5 the TCs measured higher temperatures. A decrease in measured temperature as layers are built on top of the TCs, as demonstrated by the coupon 1 data, is consistent with intuition since a greater volume has a greater heat capacity and thus a smaller temperature gradient for the same heat input. Further analysis is needed to explain the trend of increasing measured temperature in the coupon 5 TC data.

4.3 Representative results: Laser/Galvanometer data

Sample data from Tests 1 and 2 were used as representative examples of $P(t)$ because these samples illustrate the difference in signal-to-noise (SNR) level encountered at low and high laser powers, respectively. Fig. 10 shows that $P_{nom} = 6.875$ W produced a laser signal that oscillated up from 6.75 W to 9.5W with a period of roughly 1 second. The figure also shows that in Test 2, in which $P_{nom} = 275$ W, received an actual laser signal of approximately 225 W. The oscillation of the laser signal from its peak value to approximately 0 in Test 2 was due to the laser being shut off at the end of each traversal of the coupon width prior to changing directions. However, Fig. 10 illustrates that the laser never truly turned off, settling instead to a value of about 7 W.

Fig. 10 demonstrates $x_c(t)$ and $y_c(t)$. The X-Galvo rapidly oscillates between minimum and maximum x-coordinates as it rasters across the width of the coupon. The Y-Galvo signal presents a slow triangular wave as it governs the sweep down the length of the coupon. Sudden spikes in the Y-Galvo position at $t = 1$, 4 seconds of Fig. 10 are due to the G-code routine commanding the Y-Galvo to return to a "home" position prior to the beginning of each sweep.

4.4 Representative results: IR camera footage

Fig. 11 shows representative screenshots of IR camera footage. Fig. 11a is representative of build chamber camera footage during Test 1. Unique to the build camera footage of Test 1 are features besides those produced by the rastering laser such as the powder and reflected light from the tape used to hold down the TC cables. Fig. 11b is representative of build chamber camera footage during Tests 2 and 3. For properly-calibrated ε, the only visible features for this Test footage are regions of material that are at elevated temperatures due to the rastering laser. Fig. 11c is representative of melt pool camera footage during Tests 2 and 3. No representative image for Test 1 is given because the elevated temperatures during Test 1 were insufficient to produce a corresponding visible image on the melt pool camera and therefore produced seemingly-blank

footage. The melt pool camera operated with dual-color pyrometry and hence measured incident radiation intensity at two wavelengths simultaneously with two different cameras. Footage from both cameras constitutes the melt pool camera measurement output for all Tests. These images may be post-processed to recover temperature information according to the procedures given in Appendix A.

5   Summary and Conclusions

This work reviews the setup, procedures, findings, and data storage of an experiment carried out using an open-architecture laser powder bed fusion (L-PBF) system. The experiment measured internal temperature signals within parts being manufactured by the L-PBF process along with corresponding process input signals and surface temperature distributions. These tests were performed on a test part consisting of a base plate with eight raised coupons that was constructed from 304 stainless steel with thermocouples (TCs) embedded within the base plate and all coupons. This part was built to mimic a set of partially-built test coupons. The TC-embedded test part was inserted into the open architecture L-PBF machine, immersed in powder, and connected to a DAQ setup. Three tests were carried out: rastering the machine laser overtop the exposed coupon surfaces without inducing melting, rastering the machine laser overtop the exposed coupon surfaces at sufficiently high power to melt the metal, and building five layers of fresh steel on top of the exposed coupon surfaces. All data from the DAQ and IR cameras was collected during each test and is freely available to download as specified in Table 4. Representative samples of this dataset are included with this paper.

We expect this dataset to be valuable to researchers with an interest in understanding the process dynamics of L-PBF. Unlike typical L-PBF model validation studies which consider thin-walled structures or plates and measure internal temperatures in at most three locations that are far afield of the melt pool, our dataset measures internal temperatures of test coupons with complex geometry at two subsurface locations near the melt pool that were designed to generate repeat data signals in addition to two far afield measurements. Furthermore, unlike typical L-PBF model validation studies which measure data from single test coupons, our dataset provides data from two test coupon geometries with four replicates for each geometry. Our dataset includes process data for three increasingly-complex levels of process dynamics: pure heat conduction during the first test in which no metal was melted, phase change and fluid flow mechanics during the second test in which a melt pool was generated, and material addition during the last test. Our dataset is therefore valuable for validating models with a wide range of complexity. We also provide measured data of process input/output signals such as laser power, laser centroid position, and IR camera data for all tests. These input signals can be fed into process models to generate a better basis for comparing model predictions with our dataset's observed dynamics and process outputs.

Future work includes analyzing the microstructure of the coupons and presenting this data to the L-PBF community. This data will help researchers validate process models with observed microstructures for complex geometries and specified loading conditions. We also intend to leverage this dataset in future works that validate our own PBF process models. This experiments' design is

highly modular, with the procedures being repeated easily for different combinations of recorded available inputs/outputs of the open architecture machine as well as with different coupon geometries.

6 Acknowledgements

Appendix A: Calibration routines

All data corresponding to these calibrations is available with our Test data as specified in Table 4.

A.1 Emissivity calibrations

Table 6 lists the emissivity calibration tests that were performed over the course of the tests along with available data from the calibrations. All calibrations followed the procedures of Fig. 13. In summary, to calibrate ε for elevated temperatures, a test TC (the "emissivity TC") was placed on the exposed surface of a coupon and the laser rastered over the exposed surface. The emissivity TC and exposed surface were assumed isothermal when the laser rastered over the TC. Therefore by comparing the TC reading with the apparent temperature observed by the build chamber camera, one could adjust the emissivity ε value until they matched. Calibrating ε for low temperatures followed a simpler procedure. The L-PBF system was allowed to idle at ambient temperature until the system reached steady state. Fig. 12 demonstrates representative measured data from TCA-TCD for these conditions. The temperature gradient between TCA and TCC was within 1K, and as such the temperature gradient between TCA and TCB and the exposed surface was assumed to be negligible. Therefore temperature measurements from these TCs were used in lieu of a TC resting on the exposed build surface. The build chamber camera was used to measure the apparent temperature of the exposed surface, and ε was adjusted until this apparent temperature matched measurements of TCA and TCB.

A.2 Background noise calibration for coupons 5-8

As mentioned in Section 3.3, the background noise in the TC data for coupons 5-8 was unusually high. No means of eliminating this noise from the TC signals was found. It was decided to

Table 6: Emissivity ε calibration tests. All emissivity calibrations performed according to the procedures given in Fig. 13. Data is available as specified in Table 4

material	temp. range	coupon tested (j)	emissivity TC placement	applicable filename
Powder	low	0 (powder)	beneath surface	–
Wrought steel	low	3	TCs A, B (beneath surface)	–
Wrought steel	high	3	on exposed surface	wrought_emissivity_calibration_high.ravi wrought_emissivity_calibration_high.mat
Laser treated steel	low	2	TCs A, B (beneath surface)	–
Laser treated steel	high	2	on exposed surface	laser_treated_emissivity_cal_high.ravi laser_treated_emissivity_cal_high.mat
Laser treated steel	low	3	TCs A, B (beneath surface)	–
Laser treated steel	high	3	on exposed surface	laser_treated_emissivity_cal_p3_high.ravi laser_treated_emissivity_p3_cal_high.mat
Welded powder surface	low	4	TCs A, B (beneath surface)	welded_powder_emissivity_calibration_low.ravi welded_powder_emissivity_calibration_low.mat
Welded powder surface	high	4	on exposed surface	welded_powder_emissivity_calibration_high.ravi welded_powder_emissivity_calibration_high.mat

measure a sample of isolated noise data to better understand its characteristics. This was accomplished by letting the DAQ measure a stream of data while no laser rastered over the coupons. Any perturbations from a uniform temperature signal in the measured TC data streams was assumed to result from this noise. We provide this data under the filename "5-8_laser_background.mat."

A.3 melt pool camera calibration

As discussed in Section 4, the output of the melt pool camera comprised footage from two IR cameras measuring the intensity of light incident on the melt pool camera at two different wavelengths, with the IR camera corresponding to the larger wavelength being denoted as "long radiation" camera (R_1) and that corresponding to the shorter wavelength being denoted as the "short radiation" IR camera (R_2). The temperatures associated with these intensity measurements may be recovered by computing the ratio of observed measurements from the two IR cameras, $R_{12} = R_1/R_2$. Fig. 14 shows the EWI-supplied calibration points which relate R to surface temperature.

Appendix B: Tabulated experimental data

Here we tabulate available experimental data and experimental setup information. Appendix B.1 presents the available measured data for each test. Appendix B.2 contains photographs of the experimental setup. Appendix B.3 displays the nominal dimensions of the test part. Appendix B.4 lists the measured dimensions of the test part.

B.1 Available measurements

Table 7 lists the available measurements for all tests performed during this work.
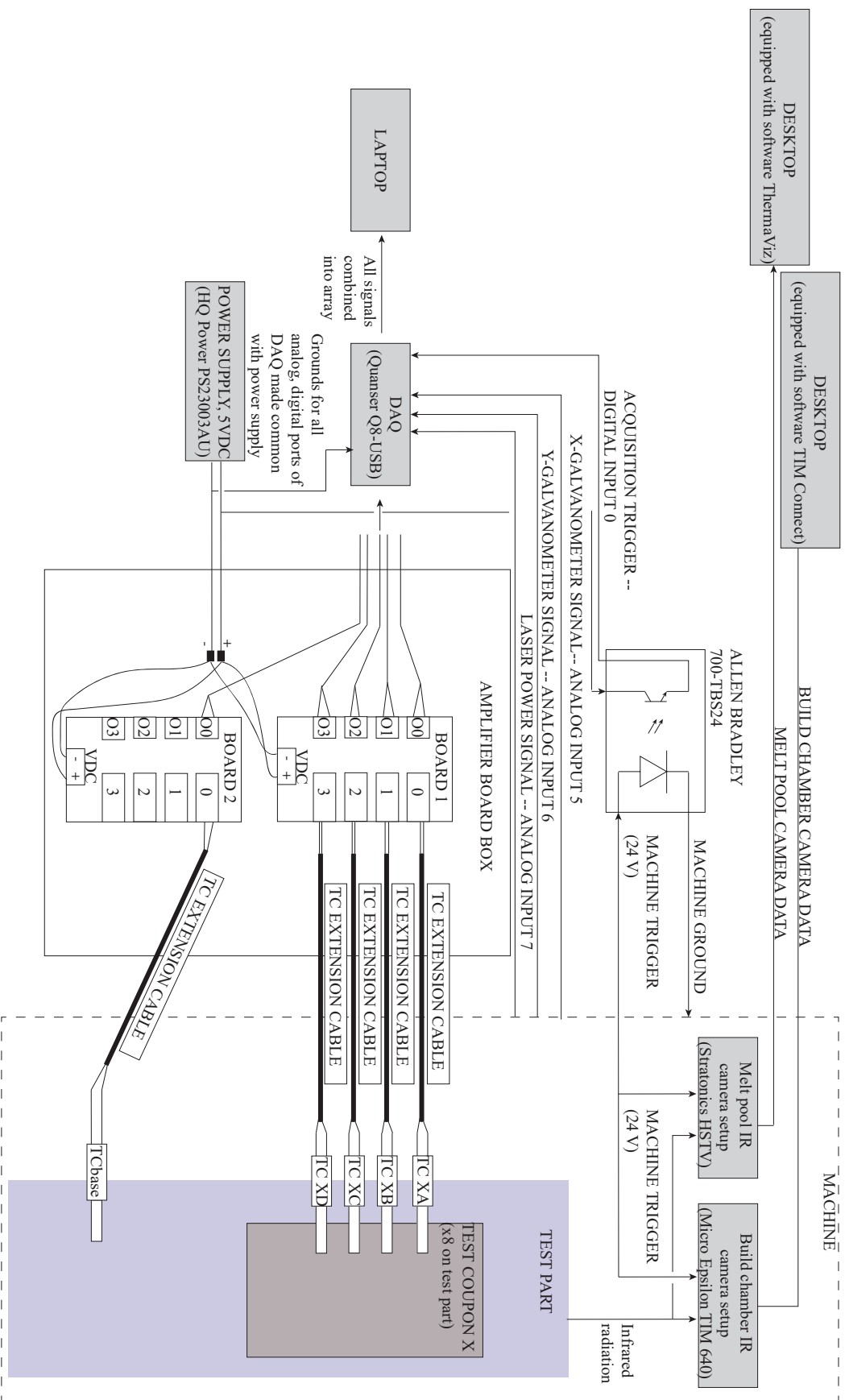
Figure 4: **Wiring diagram of experimental setup**
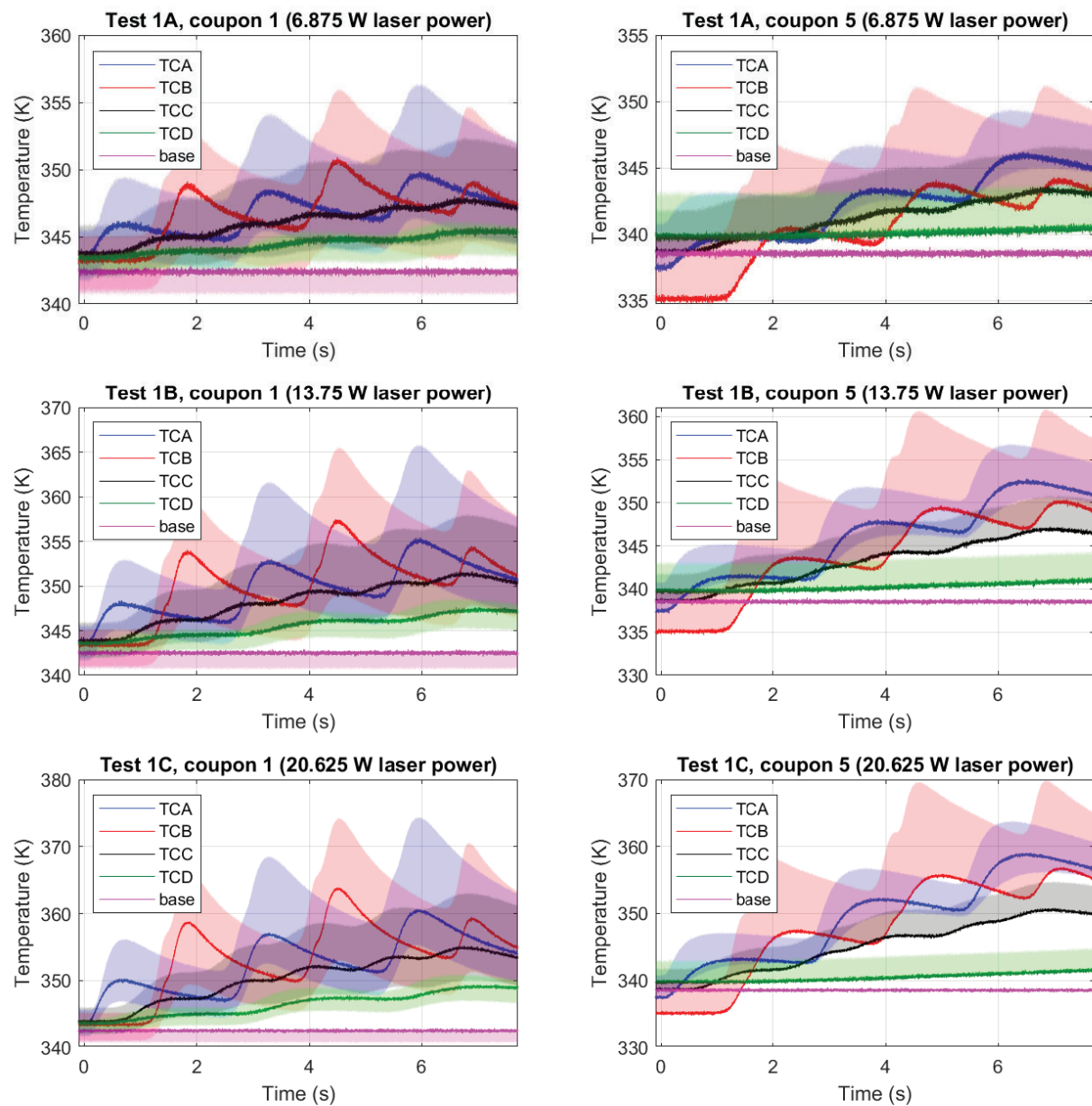
Figure 5: TC signal data from coupons 1 and 5, Test 1. Shaded envelopes denote bounds of minimum and maximum recorded values for all TC signals within replicate sets 1-4 or 5-8, as applicable.
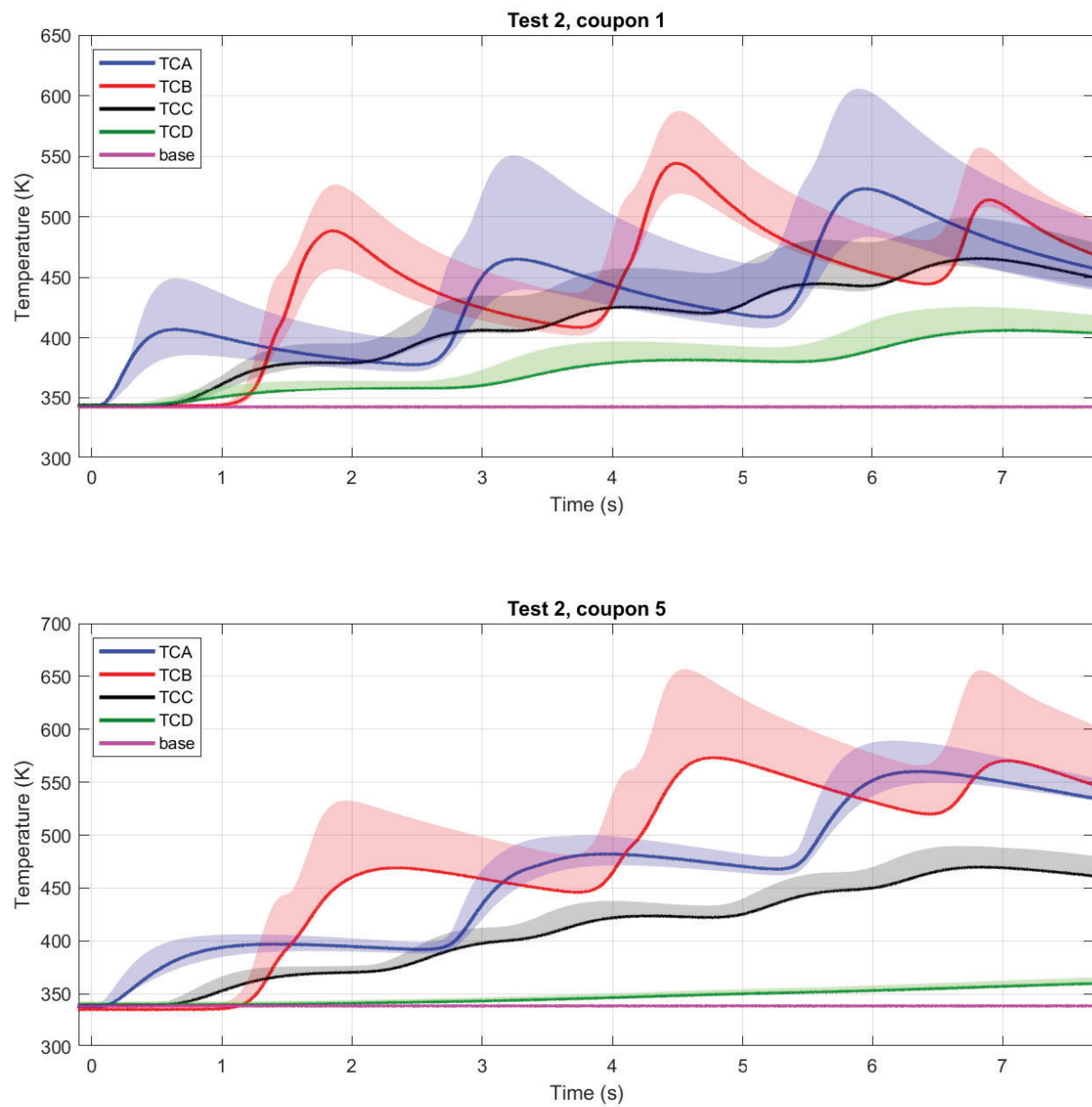
Figure 6: TC signal data from coupons 1 and 5, Test 2. Shaded envelopes denote bounds of minimum and maximum recorded values for all TC signals within replicate sets 1-4 or 5-8, as applicable.
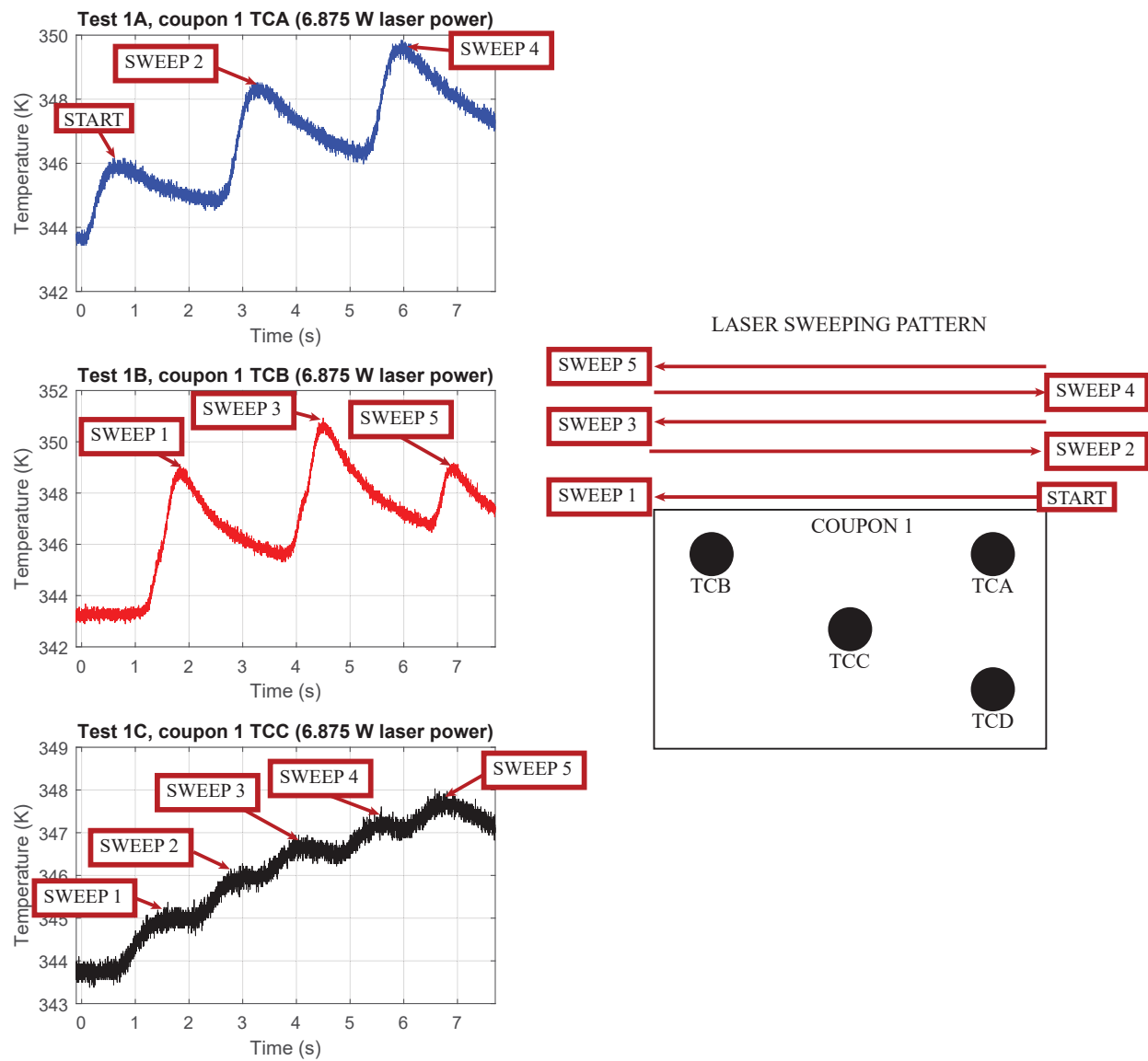
Figure 7: Relationship between sweeping pattern of machine laser and subsequent peaks of TC signal
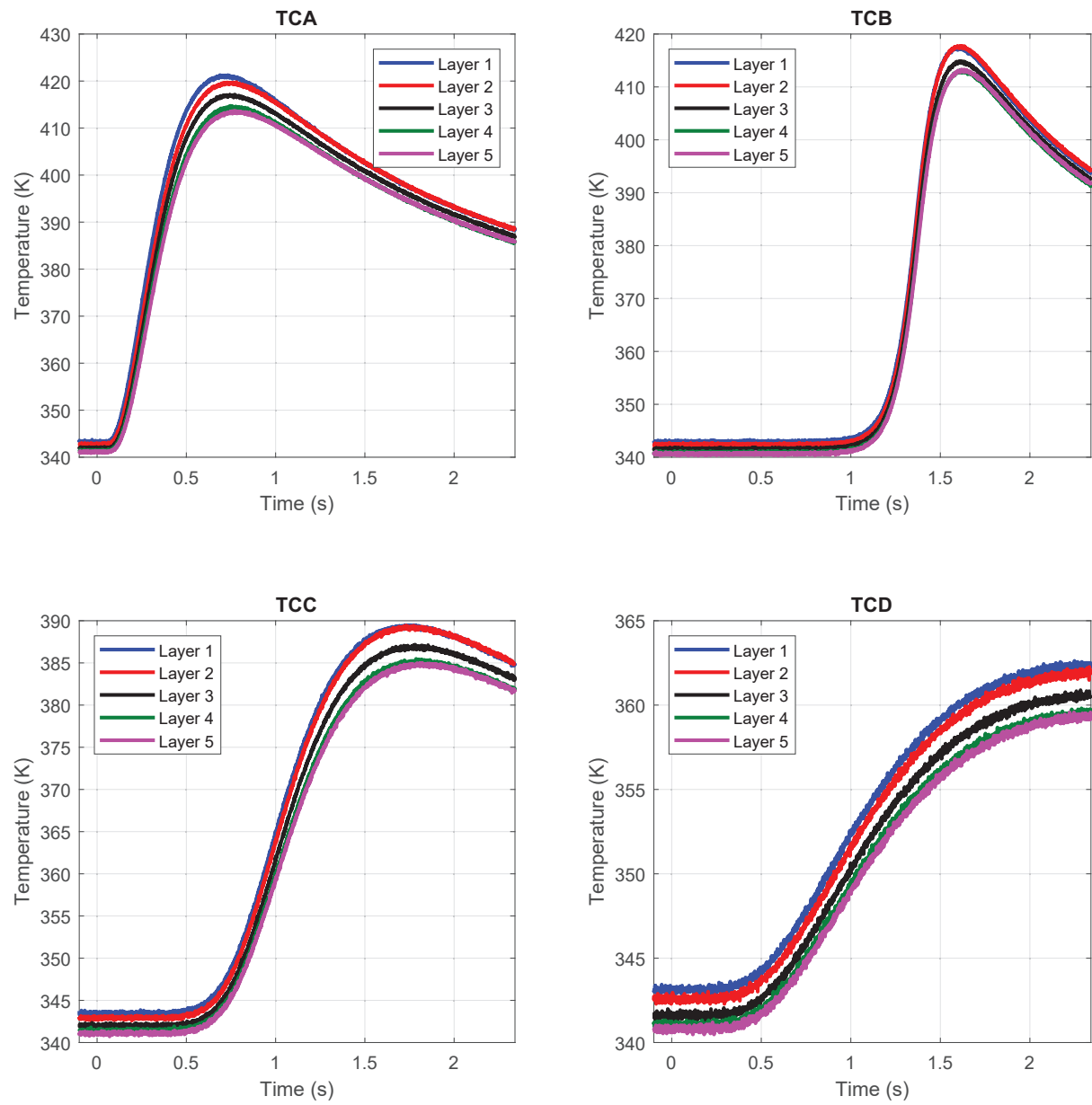
Figure 8: TC signal data from coupon 1, Test 3
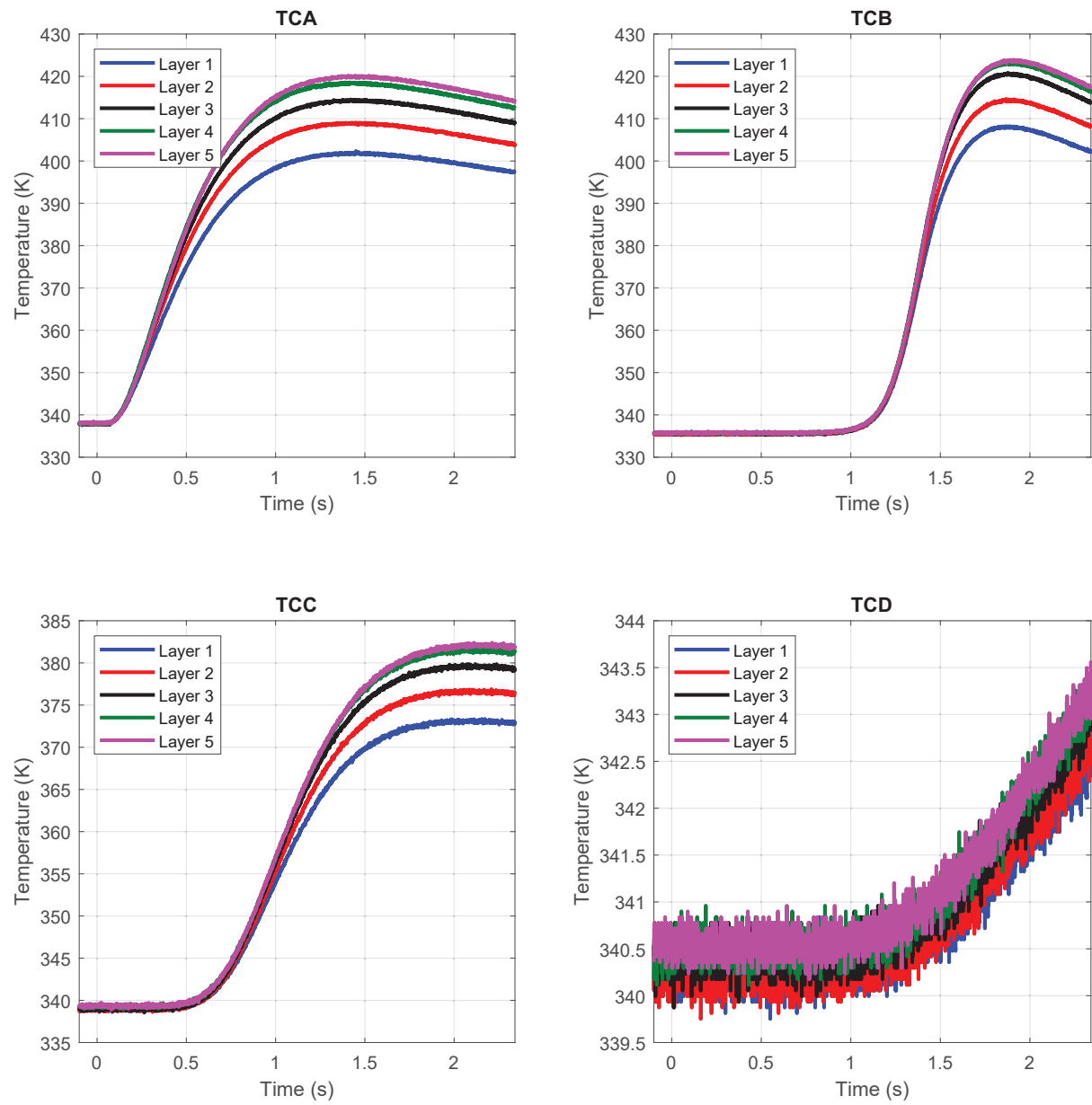
Figure 9: TC signal data from coupon 5, Test 3
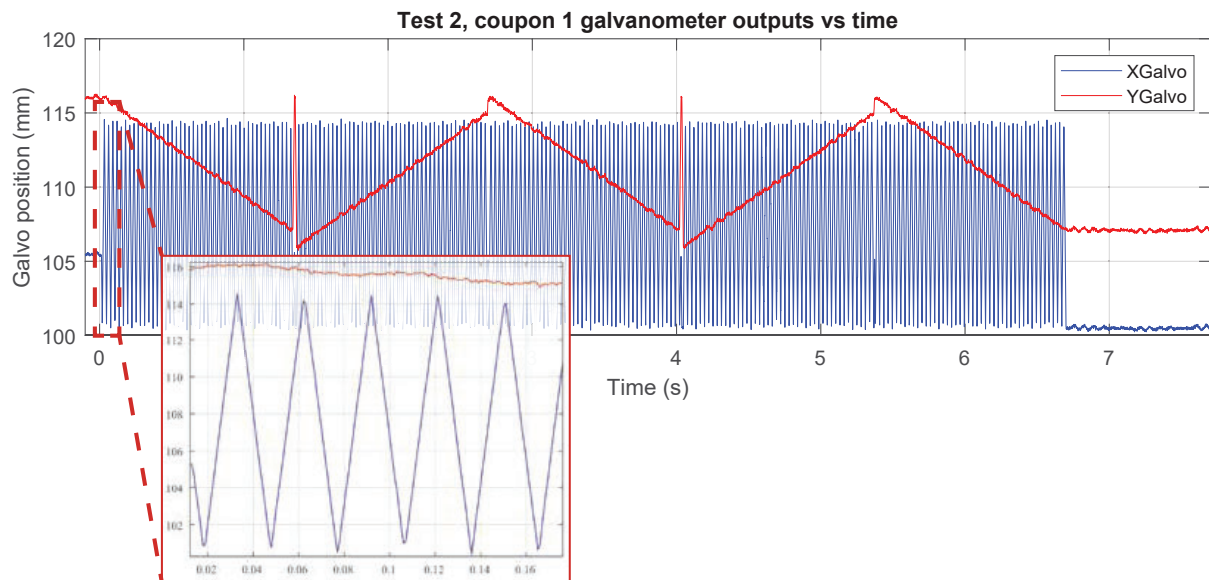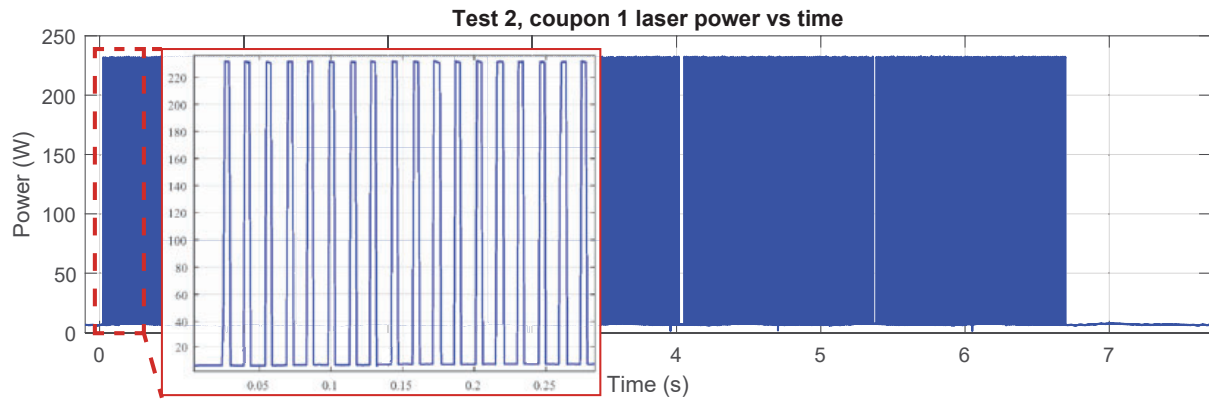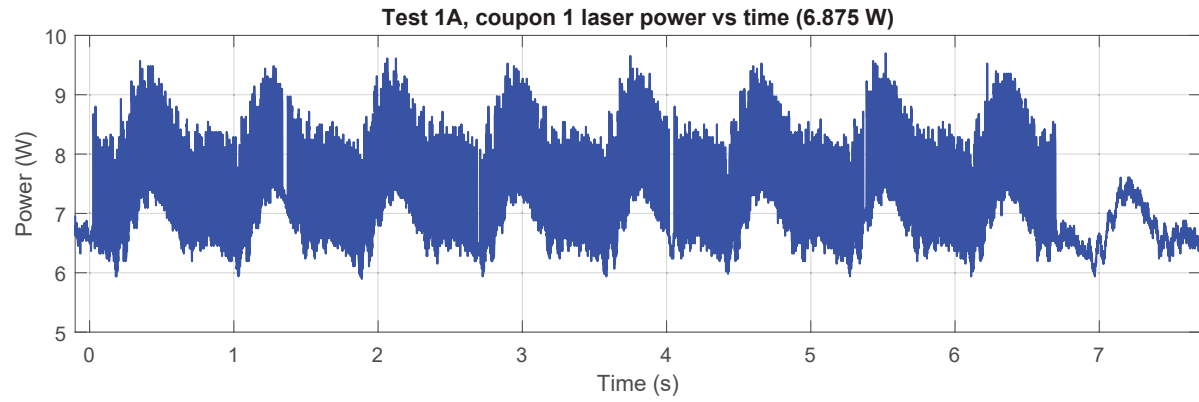
Figure 10: Representative laser power and laser centroid signals.
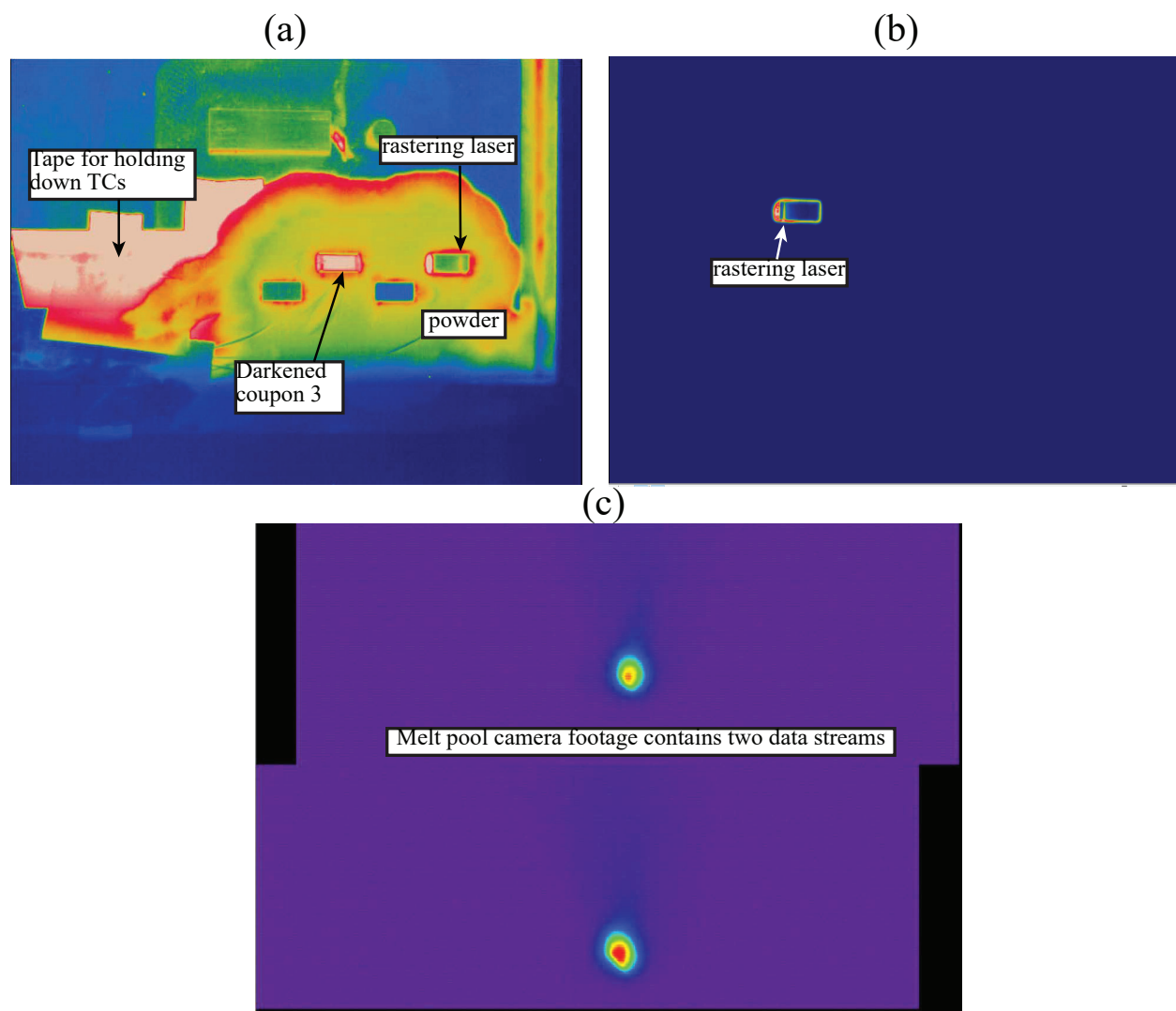
Figure 11: **Representative screenshots of IR camera footage.** (a) Build chamber camera footage, Test 1c, coupon 1. (b) Build chamber camera footage, Test 2, coupon 5. (c) Melt pool camera footage, Test 2, coupon 1.
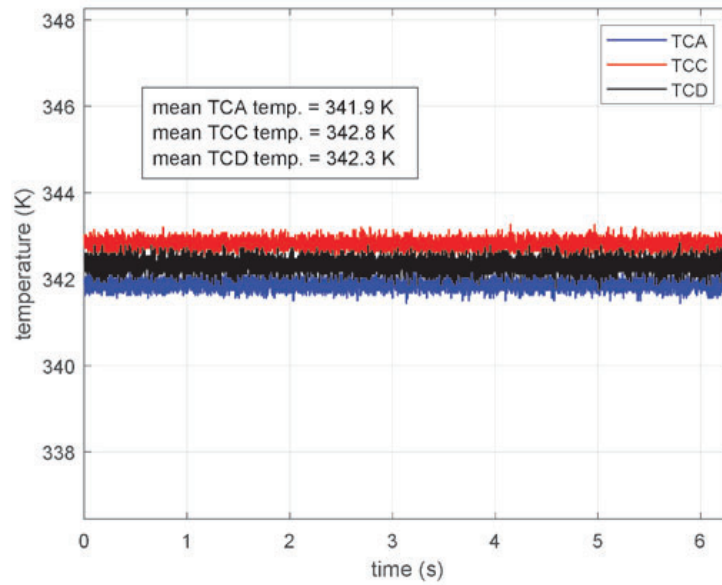
Figure 12: **Representative low temperature ε TC calibration data** Data corresponds to ε calibration for the welded powder surface of coupon 4 at low temperatures. TCB data is absent as noted in Section 3.3.

Emissivity calibrations

Low temp.

start

Allow coupon j to settle to ambient temperature conditions

Measure temperatures ofTCs A and B of coupon j, assumed at same temperature as exposed coupon surface

Measure temperature of exposed build surface using build chamber IR camera

Adjust emissivity value of build chamber IR camera until apparent temperature matches that displayed by TCs

end

High temp.

start

Place TC on exposed surface of coupon j, termed "emissivity TC"

Run High Temp. Emissivity Calibration Scan, collecting IR data and data f rom Emissivity TC

Adjust emissivity value of build chamber IR camera until temperatues measured by IR camera and Emissivity TC match wehen laser passes over Emissivity TC

end

Figure 13: Flowchart of procedure for testing the emissivity of coupon surfaces. The scan "High Temp. Emissivity Calibration Scan" is specified in Fig. 2 and Table 1.

Figure 14: **Melt pool camera calibration**: Calibration points correlating known surface temperature with R_{12}.

Table 7: Data table. X marks data available for the given test, numbered according to Section 3. Orange squares mark unavailable data. Measurements numbered according to Fig. 1.

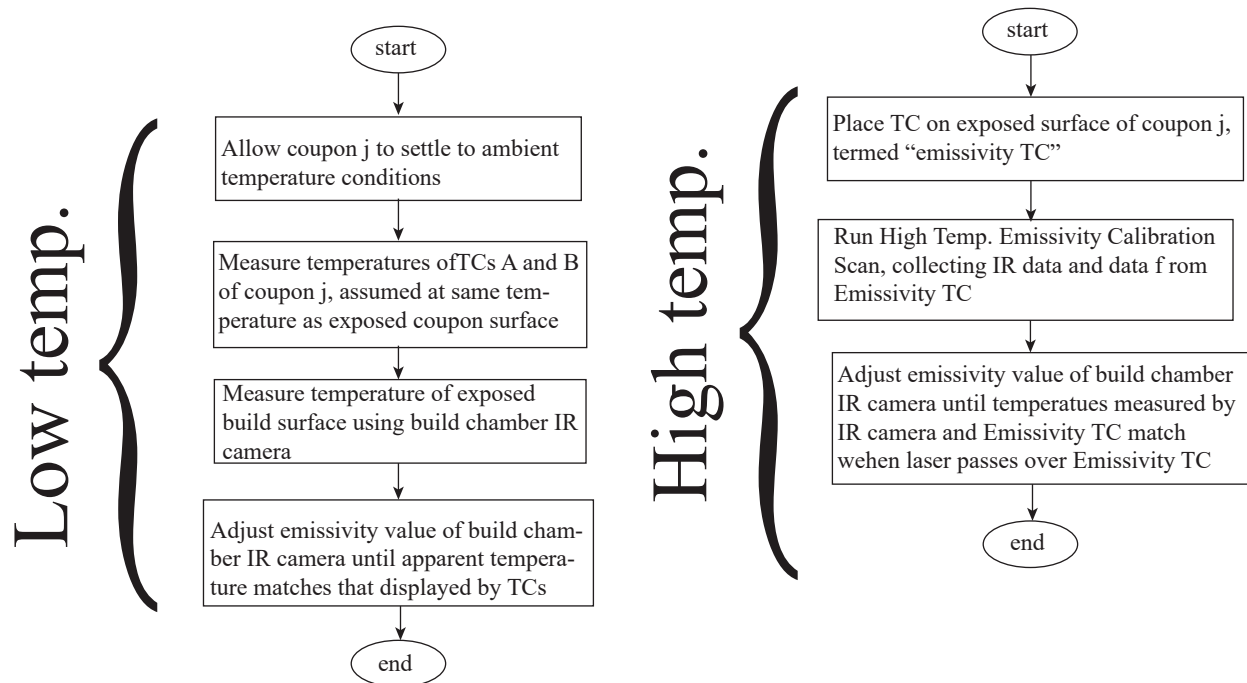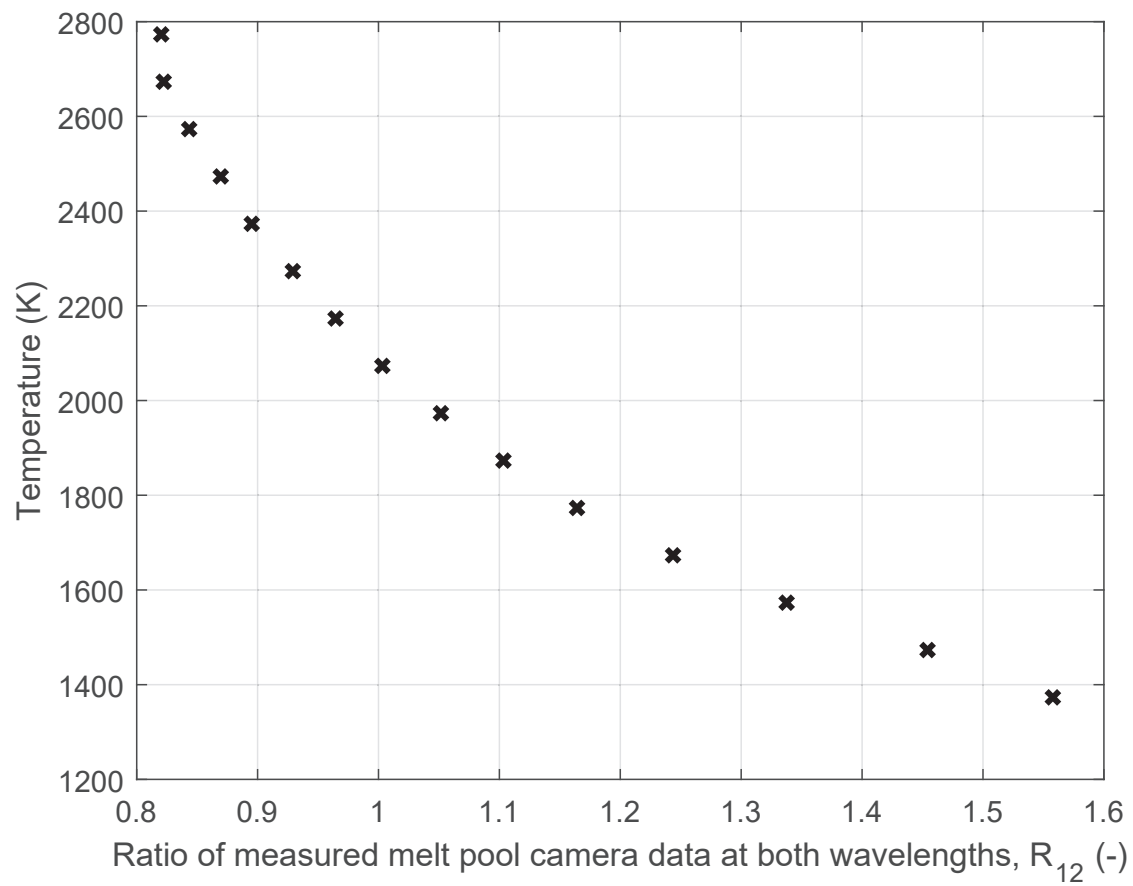| Test	coupon		1	2	3	4	5	6	7	8	9	10	11	12
1A	replicate	1	X	X	X	X	X	X	X	X	X	X	X	X
		2	X	X	X	X	X	X	X	X	X	X	X	X
		3	X	X	X	X	□	X	X	X	X	X	X	X
		4	X	X	□	X	X	X	X	X	X	X	X	X
		5	X	X	X	X	X	X	X	X	X	X	X	X
	replicate	6	X	X	□	X	X	X	X	X	X	X	X	X
		7	X	X	X	X	X	X	X	X	X	X	X	X
		8	X	X	X	X	X	X	X	X	X	X	X	X
1B	replicate	1	X	X	X	X	X	X	X	X	X	X	X	X
		2	X	X	X	X	X	X	X	X	X	X	X	X
		3	X	X	X	X	□	X	X	X	X	X	X	X
		4	X	X	□	X	X	X	X	X	X	X	X	X
		5	X	X	X	X	X	X	X	X	X	X	X	X
	replicate	6	X	X	□	X	X	X	X	X	X	X	X	X
		7	X	X	X	X	X	X	X	X	X	X	X	X
		8	X	X	X	X	X	X	X	X	X	X	X	X
1C	replicate	1	X	X	X	X	X	X	X	X	X	X	X	X
		2	X	X	X	X	X	X	X	X	X	X	X	X
		3	X	X	X	X	□	X	X	X	X	X	X	X
		4	X	X	□	X	X	X	X	X	X	X	X	X
		5	X	X	X	X	X	X	X	X	X	X	X	X
	replicate	6	X	X	□	X	X	X	X	X	X	X	X	X
		7	X	X	X	X	X	X	X	X	X	X	X	X
		8	X	X	X	X	X	X	X	X	X	X	X	X
2	replicate	1	X	X	X	X	X	X	X	X	X	X	X	X
		2	X	X	X	X	X	X	X	X	X	X	X	X
		3	X	X	X	X	□	X	X	X	X	X	X	X
		4	X	X	□	X	X	X	X	X	X	X	X	□
		5	X	X	X	X	X	X	X	X	X	X	X	X
	replicate	6	X	X	□	X	X	X	X	X	X	X	X	X
		7	X	X	X	X	X	X	X	X	X	X	X	X
		8	X	X	X	X	X	X	X	X	X	X	X	X
3, Layer 1	replicate	1	X	X	X	X	X	X	X	X	X	X	X	X
		2	X	X	X	X	X	X	X	X	X	X	X	X
		3	X	X	X	X	□	X	X	X	X	X	X	X
		4	X	X	□	X	X	X	X	X	X	X	X	X
		5	X	X	X	X	X	X	X	X	X	X	X	X
	replicate	6	X	X	□	X	X	X	X	X	X	X	X	X
		7	X	X	X	X	X	X	X	X	X	X	X	X
		8	X	X	X	X	X	X	X	X	X	X	X	X

|		1	2	3	4	5	6	7	8	9	10	11	12
3, Layer 2	replicate 1	X	X	X	X	X	X	X	X	X	X	X	X
	2	X	X	X	X	X	X	X	X	X	X	X	X
	3	X	X	X	X	▮	X	X	X	X	X	X	X
	4	X	X	▮	X	X	X	X	X	X	X	X	X
	replicate 5	X	X	X	X	X	X	X	X	X	X	X	X
	6	X	X	▮	X	X	X	X	X	X	X	X	X
	7	X	X	X	X	X	X	X	X	X	X	X	X
	8	X	X	X	X	X	X	X	X	X	X	X	X
3, Layer 3	replicate 1	X	X	X	X	X	X	X	X	X	X	X	X
	2	X	X	X	X	X	X	X	X	X	X	X	X
	3	X	X	X	X	▮	X	X	X	X	X	X	X
	4	X	X	▮	X	X	X	X	X	X	X	X	X
	replicate 5	X	X	X	X	X	X	X	X	X	X	X	▮
	6	X	X	▮	X	X	X	X	X	X	X	X	X
	7	X	X	X	X	X	X	X	X	X	X	X	X
	8	X	X	X	X	X	X	X	X	X	X	X	X
3, Layer 4	replicate 1	X	X	X	X	X	X	X	X	X	X	X	X
	2	X	X	X	X	X	X	X	X	X	X	X	X
	3	X	X	X	X	▮	X	X	X	X	X	X	X
	4	X	X	▮	X	X	X	X	X	X	X	X	▮
	replicate 5	X	X	X	X	X	X	X	X	X	X	X	X
	6	X	X	▮	X	X	X	X	X	X	X	X	X
	7	X	X	X	X	X	X	X	X	X	X	X	X
	8	X	X	X	X	X	X	X	X	X	X	X	X
3, Layer 5	replicate 1	X	X	X	X	X	X	X	X	X	X	X	X
	2	X	X	X	X	X	X	X	X	X	X	X	X
	3	X	X	X	X	▮	X	X	X	X	X	X	X
	4	X	X	▮	X	X	X	X	X	X	X	X	X
	replicate 5	X	X	X	X	X	X	X	X	X	X	X	X
	6	X	X	▮	X	X	X	X	X	X	X	X	X
	7	X	X	X	X	X	X	X	X	X	X	X	X
	8	X	X	X	X	X	X	X	X	X	X	X	X
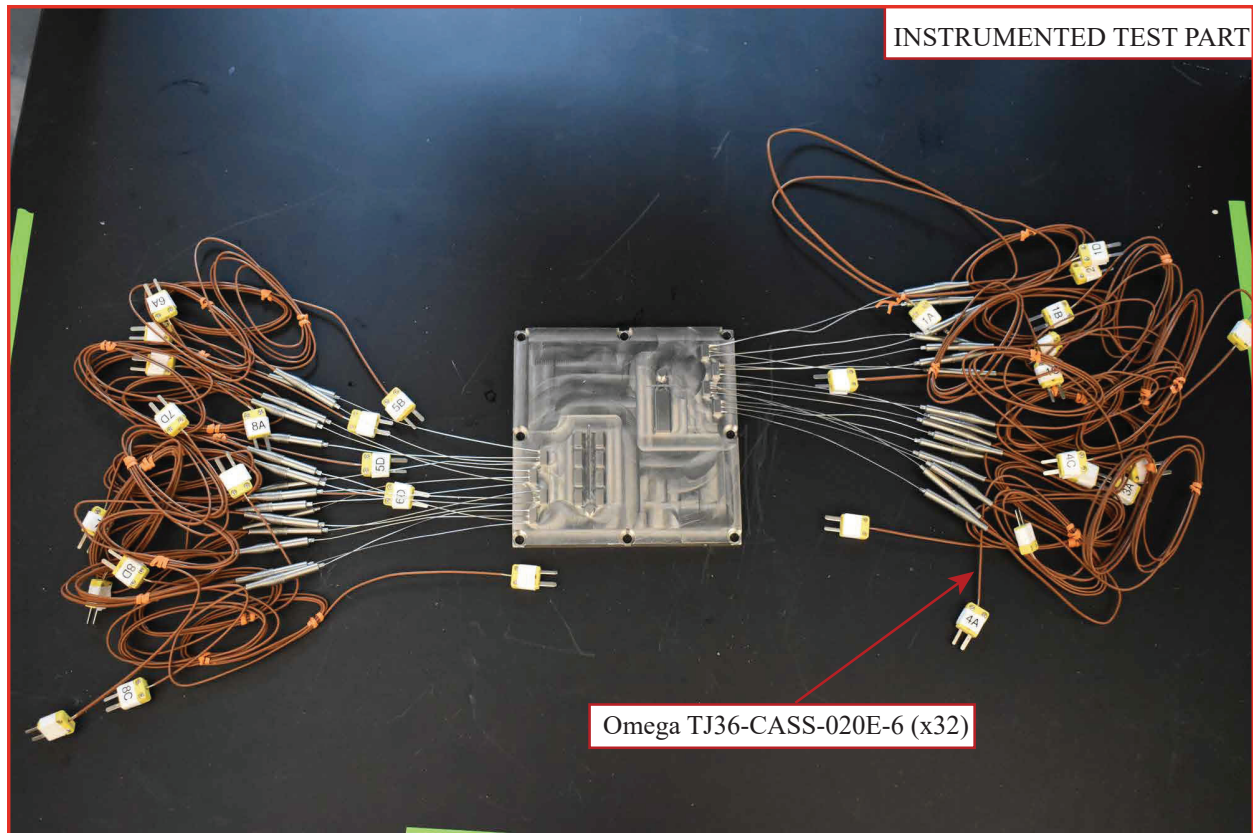
Figure 15: **Photograph of test part with embedded TCs**

B.2 Photographs of Experimental setup

We provide the following figures of our experimental setup:

- Fig. 15 shows the configuration of the test part with embedded TCs.

- Fig. 16 shows the configuration of the test part within the EWI open source PBF machine during testing on coupons 1-4.

- Fig. 17 shows the configuration of the test part within the EWI open source PBF machine during testing on coupons 5-8.

B.3 Nominal dimensions of test part

Fig. 18 demonstrates the nominal dimensions of all features within the test part.

(a)

Extension cables to DAQ

TCs connected to their extensions

test part

Base plate TC: Omega TJ36-CASS-18U-6

gas orifice

Tape down TCs to avoid recoater blade

(b)

Coupons 1-4 immersed in powder to complete Tests 1, 2

(c)

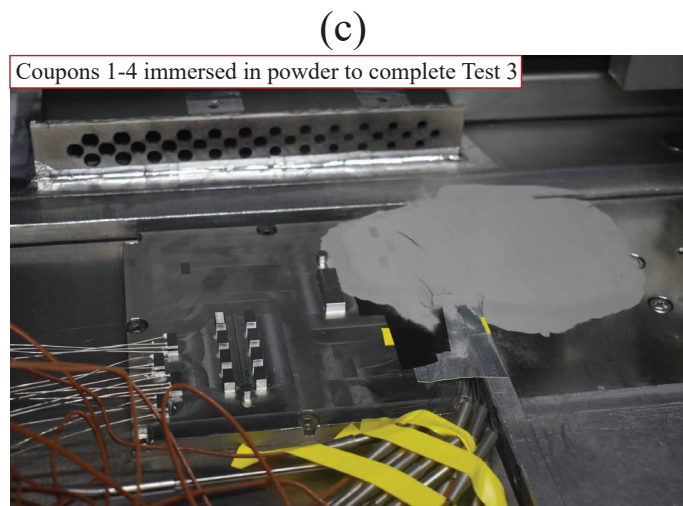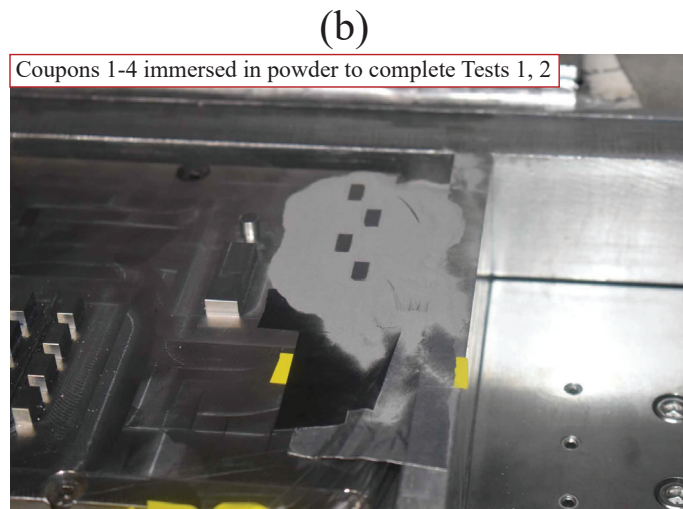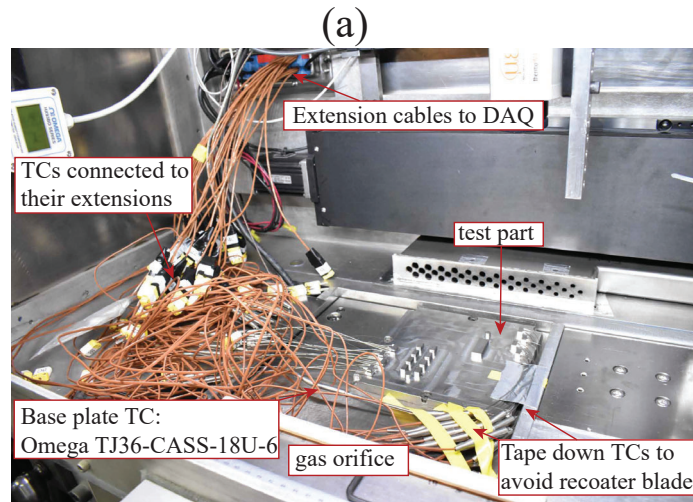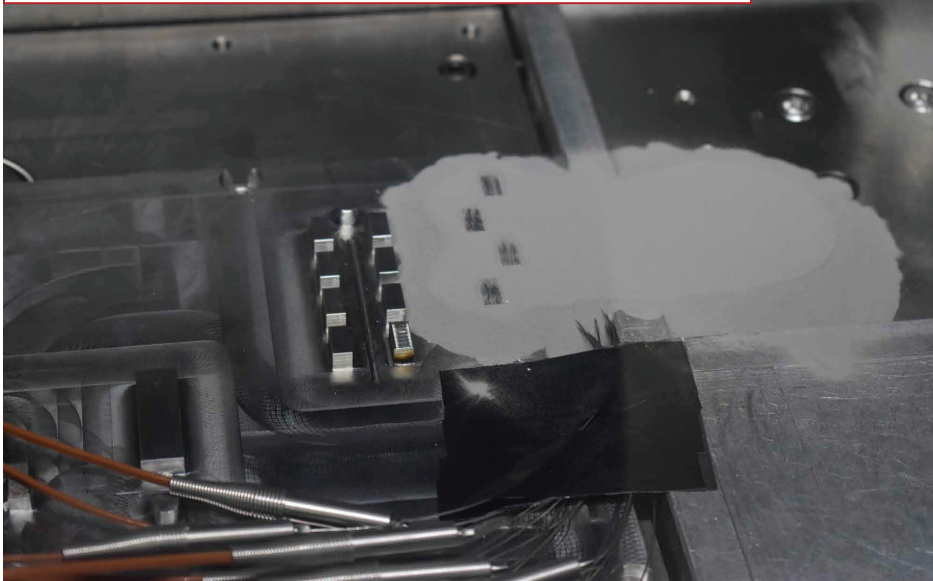Coupons 1-4 immersed in powder to complete Test 3

Figure 16: **Placement of test part in machine for running Tests on coupons 1-4:** (a): general location of test part in machine, relative to TC extension cables. (b) Coupons 1-4 immersed in powder for completing Tests 1, 2. (c) Coupons 1-4 covered by powder for completing Test 3.

(a)
Coupons 5-8 immersed in powder to complete Tests 1, 2

(b)
Coupons 5-8 covered in powder to complete Test 3
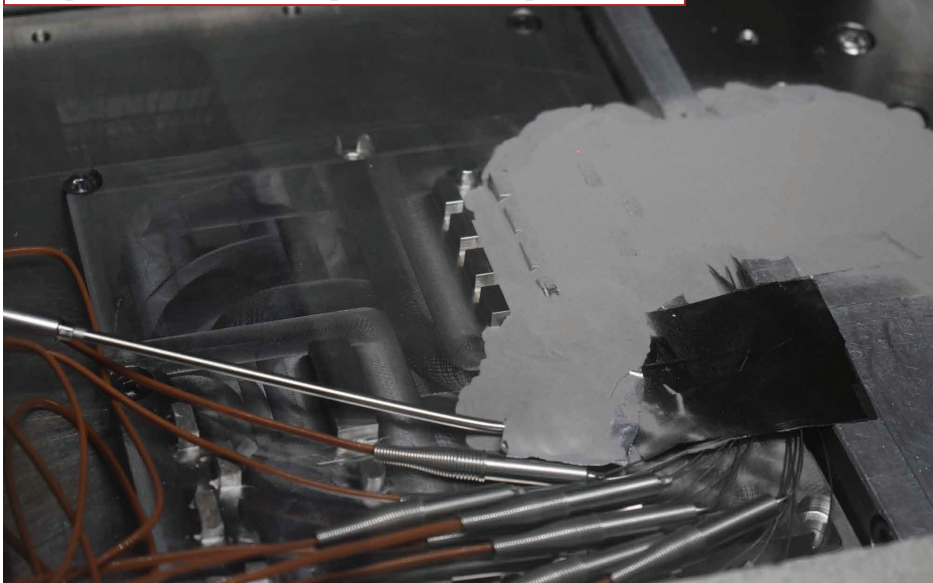
Figure 17: **Placement of test part in machine for running Tests on coupons 5-8:** (a) Coupons 5-8 immersed in powder for completing Tests 1, 2. (b) Coupons 5-8 covered by powder for completing Test 3.

B.4 Measured dimensions of test part

The dimensions of all features of the test part were measured by Selecteon Corporation after manufacturing. Fig. 19 displays the feature labeling convention used by Selecteon when reporting

Figure 18: Engineering drawing of test part with all nominal dimensions labeled.

1476

their findings. Tb. 8 lists these dimensions.
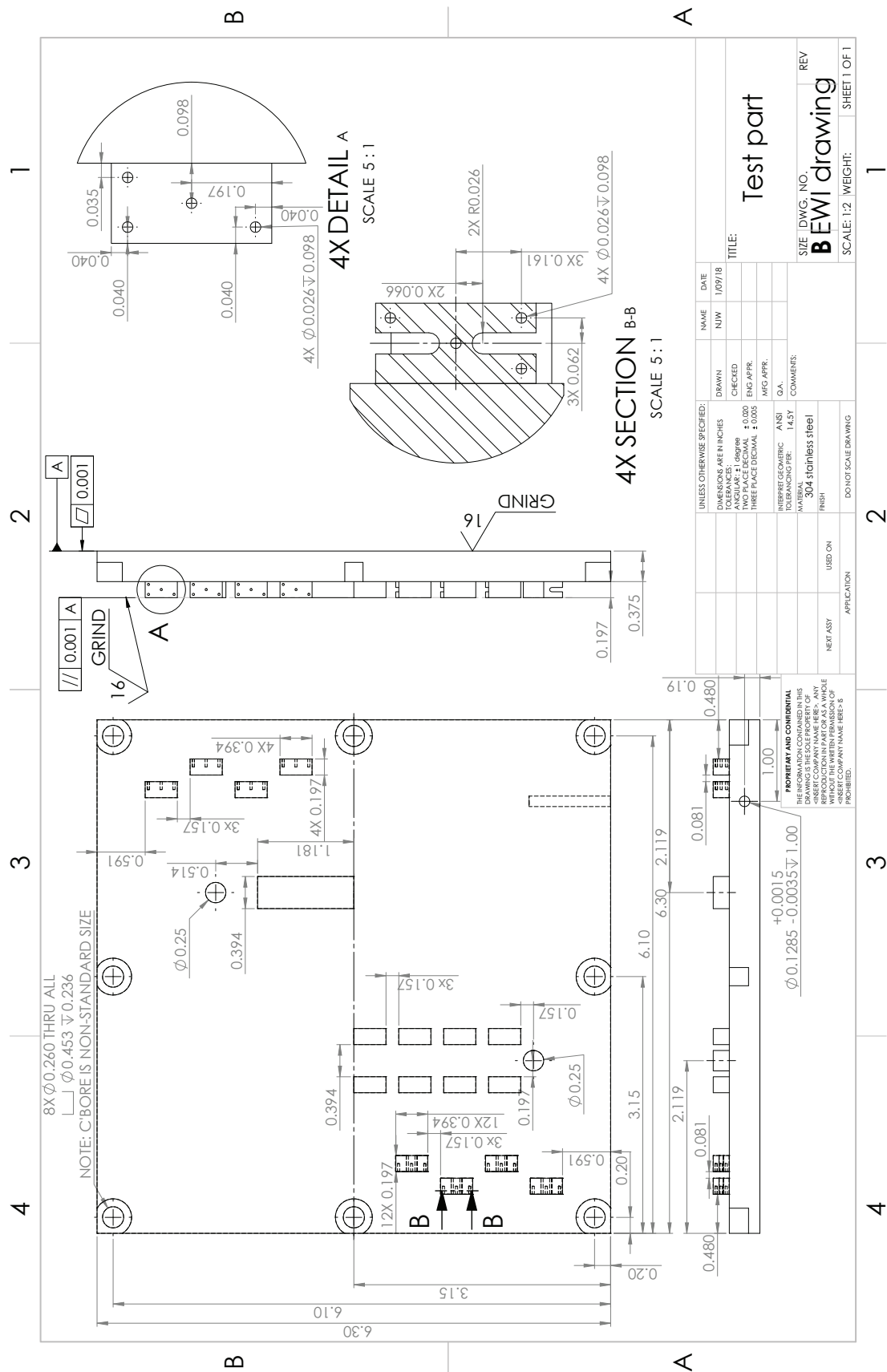
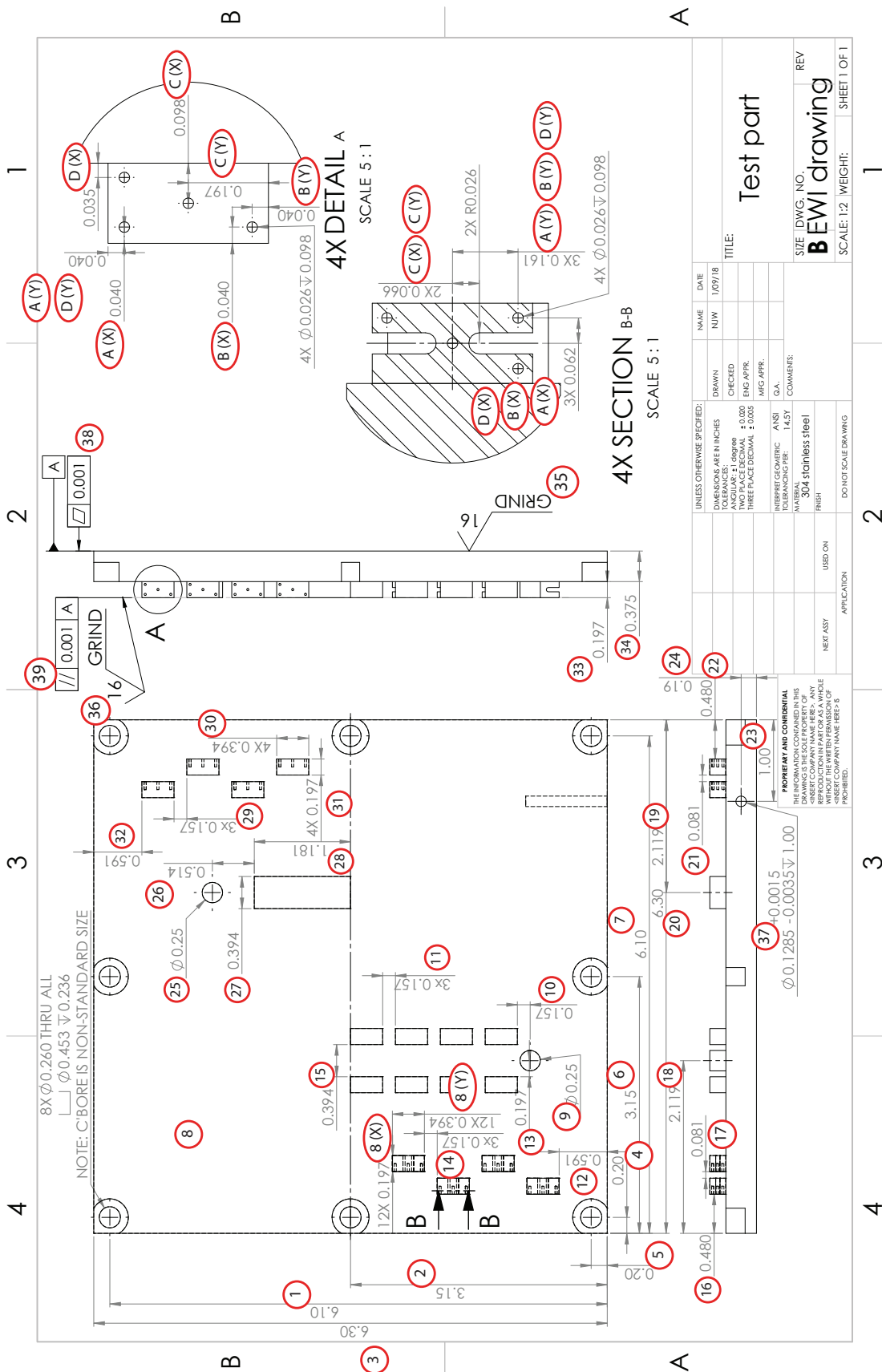Table 8: Measured dimensions of test part. Numbers in reference to Fig. 19. Dimensions in inches.

Dimension	value	Dimension	value	Dimension	value
1	6.108	32	0.587	8A (X)	0.0630
2	3.156	33	0.197	8A (Y)	0.1601
3	6.301	34	0.377	8B (X)	0.0609
4	0.196	35	11.2	8B (Y)	0.1611
5	0.201	36	10.2	8C (X)	0.0712
6	3.149	37 (diameter)	0.127	8C (Y)	0.0623
7	6.102	37 (depth)	0.982	8D (X)	0.0605
	0.191	38	0.0005	8D (Y)	0.1606
	0.189	39	0.0029		
	0.191	1A (X)	0.0396		
	0.190	1A (Y)	0.0320		
	0.190	1B (X)	0.0406		
8 (X) (x12)	0.191	1B (Y)	0.0426		
	0.190	1C (X)	0.098		
	0.191	1C (Y)	0.1997		
	0.191	1D (X)	0.0333		
	0.191	1D (Y)	0.0307		
	0.191	2A (X)	0.0390		
	0.191	2A (Y)	0.0402		
	0.387	2B (X)	0.0405		
	0.388	2B (Y)	0.0404		
	0.388	2C (X)	0.0989		
	0.388	2C (Y)	0.1972		
	0.387	2D (X)	0.0322		
	0.387	2D (Y)	0.0409		
8 (Y) (x12)	0.387	3A (X)	0.0401		
	0.387	3A (Y)	0.0609		
	0.388	3B (X)	0.0405		
	0.387	3B (Y)	0.0406		
	0.388	3C (X)	0.0980		
	0.387	3C (Y)	0.1974		
9	0.244	3D (X)	0.0359		
10	0.160	3D (Y)	0.0610		
	0.1627	4A (X)	0.0397		
11 (x3)	0.1625	4A (Y)	0.0388		
	0.1631	4B (X)	0.0408		
12	0.6018	4B (Y)	0.0382		
13	0.200	4C (X)	0.0988		
	0.1627	4C (Y)	0.1936		
14 (x3)	0.1627	4D (X)	0.0556		

	0.1627	4D (Y)	0.0407
15	0.3997	5A (X)	0.0583
16	0.483	5A (Y)	0.1623
17	0.087	5B (X)	0.0612
18	2.120	5B (Y)	0.1608
19	2.113	5C (X)	0.0655
20	6.301	5C (Y)	0.0685
21	0.0875	5D (X)	0.0620
22	0.4766	5D (Y)	0.1611
23	0.9988	6A (X)	0.0612
24	0.183	6A (Y)	0.1608
25	0.243	6B (X)	0.0570
26	0.516	6B (Y)	0.1619
27	0.388	6C (X)	0.0674
28	1.173	6C (Y)	0.0658
	0.164	6D (X)	0.0629
29 (x3)	0.164	6D (Y)	0.1613
	0.164	7A (X)	0.0662
	0.387	7A (Y)	0.1602
30 (x4)	0.388	7B (X)	0.0638
	0.387	7B (Y)	0.1615
	0.387	7C (X)	0.0750
	0.193	7C (Y)	0.0590
	0.191	7D (X)	0.0591
31 (x4)	0.192	7D (Y)	0.1603
	0.191		

References

[1] H. Peng, M. Ghasri-Khouzani, S. Gong, R. Attardo, P. Ostiguy, B. Gatrell, B. J., C. Tomonto, J. Neidig, M. Shankar, R. Billo, D. Go, and D. Hoelzle, "Fast prediction of thermal distortion in metal powder bed fusion additive manufacturing: Part 1, a thermal circuit network model," *Additive Manufacturing*, vol. 22, pp. 852–868, 2018.

[2] ——, "Fast prediction of thermal distortion in metal powder bed fusion additive manufacturing: Part 2, a quasi-static thermo-mechanical model," *Additive Manufacturing*, vol. 22, pp. 869–882, 2018.

[3] T. Krol, C. Seidel, J. Schilp, M. Hofmann, W. Gan, and M. Zaeh, "Verification of structural simulation results of metal-based additive manufacturing by means of neutron diffraction," *Physics Procedia*, vol. 41, pp. 849 – 857, 2013, lasers in Manufacturing (LiM 2013).

Figure 19: Engineering drawing of test part. Dimensions numbered according to dimensional layout performed by Selecteon Corporation. Dimensions for holes labeled A-D in Details A and B follow the coupon numbering convention given in Fig. 3

[4] P. K. Gokuldoss, S. Kolla, and J. Eckert, "Additive manufacturing processes: Selective laser melting, electrong beam melitng and binder jetting – selection guidelines," *Materials (Basel)*, vol. 10, no. 6, June 2017.

[5] T. DebRoy, H. Wei, J. Zuback, T. Mukherjee, J. Elmer, J. Milewski, A. Beese, A. Wilson-Heid, A. De, and W. Zhang, "Additive manufacturing of metallic components – process, structure and properties," *Progress in Materials Science*, vol. 62, pp. 112–224, 2017.

[6] T. Mower and M. Long, "Mechanical behavior of additive manufactured, powder-bed laser-fused materials," *Materials Science and Engineering: A*, vol. 651, pp. 198–213, 2016.

[7] J. Keist and T. Palmer, "Role of geometry on properties of additively manufactured ti-6al-4v structures fabricated using laser based directed energy deposition," *Materials and Design*, vol. 106, pp. 482–494, 2016.

[8] T. Wang, Y. Zhu, S. Zhang, and H. Wand, "Grain morphology evolution behavior of titanium alloy components during laser melting deposition additive manufacturing," *Journal of Alloys and Compounds*, vol. 632, pp. 505–513, 2015.

[9] H. Wei, J. Elmer, and T. DebRoy, "Origin of grain orientation during solidification of an aluminum alloy," *Acta Materialia*, vol. 115, pp. 123–131, 2016.

[10] A. Yadollahi, N. Shamsaei, S. Thompson, and D. Seely, "Effects of process time interval and heat treatment on the mechanical and microstructural properties of direct laser deposited 316l stainless steel," *Materials Science and Engineering: A*, vol. 644, pp. 171–183, 2015.

[11] L. Parimi, A. R. G., D. Clark, and M. Attallah, "Microstructural and texture development in direct laser fabricated in718," *Materials Characterization*, vol. 89, pp. 102–111, 2014.

[12] I. Roberts, C. Wang, R. Esterlein, M. Stanford, and D. Mynors, "A three-dimensional finite element analysis of the temperature field during laser melting of metal powders in additive layer manufacturing." *International Journal of Machine Tools and Manufacture*, vol. 49, pp. 916–923, 2009.

[13] S. Kolossov, E. Boillat, R. Glardon, P. Fischer, and M. Locher, "3d fe simulation for temperature evolution in the selective laser sintering process." *International Journal of Machine Tools and Manufacture*, vol. 44, pp. 117–123, 2004.

[14] P. Peyre, P. Aubry, R. Fabbro, R. Neveu, and A. Longuet, "Analytical and numerical modeling of the direct metal deposition laser process," *Journal of Physics D: Applied Physics*, vol. 41, p. 025403, 2008.

[15] A. Plati, J. Tan, O. Golosnoy, R. Persoons, K. van Acker, and T. Clyne, "Residual stress generation during laser cladding of steel with a particulate metal matrix composite," *Advanced Engineering Materials*, vol. 8, pp. 619–624, 2006.

[16] J. Heigel, P. Michaleris, and E. Reutzel, "Thermo-mechanical model development and validation of directed energy deposition additive manufacturing of ti-6al-4v," *Additive Manufacturing*, vol. 5, pp. 9–19, 2015.

[17] E. Denlinger, V. Jagdale, G. Srinivasan, T. El-Wardany, and P. Michaleris, "Thermal modeling of inconel 718 processed with powder bed fusion and experimental validation using in situ measurements," *Additive Manufacturing*, vol. 11, pp. 7–15, 2016.

[18] E. Denlinger, M. Gouge, J. Irwin, and P. Michaleris, "Thermomechanical model development and in situ experimental validation of the laser powder-bed fusion process," *Additive Manufacturing*, vol. 16, pp. 73–80, 2017.

[19] A. Dunbar, E. Denlinger, J. Heigel, P. Michaleris, P. Guerrier, R. Martukanitz, and T. Simpson, "Development of experimental method of in situ distortion and temperature measurements during the laser powder bed fusion additive manufacturing process," *Additive Manufacturing*, vol. 12, pp. 25–30, 2016.

[20] F. Cverna, Ed., *Thermal Properties of Metals*.   ASM International, 2002.

[21] A. Rich, "Shielding and guarding," *Analog Dialogue*, vol. 17, pp. 124–129, 1983.

[22] C. Roger, S. Yen, and K. Ramanthan, "Temperature variation of total hemispherical emissivity of stainless steel aisi 304."

[23] Y. Touloukian and D. DeWitt, *Thermophysical Properties of Matter*.   IFI/Plenium, 1970, vol. 7, ch. 3, p. 1210.